nature communications

Article

https://doi.org/10.1038/s41467-025-66788-4

Tumor agnostic drug delivery with dynamic nanohydrogels

Received: 18 April 2025

Accepted: 13 November 2025

Published online: 07 January 2026

Check for updates

Stephen N. Housley[1,2,3,4] ✉, Alisyn R. Bourque[4,5], Lilya V. Matyunina[1], Isabel A. Panicker[6], Elisa Schrader Echeverri[7], Marrissa Izykowicz[8], Olivia A. Herrmann[1], Sebinne Lee[1], Johana C. Arboleda[9], Vida Jamali[6], John F. McDonald[1], James E. Dahlman[7] & M. G. Finn[1,4,8]

RNA interference (RNAi) holds unique potential as a clinically viable modality to pharmacologically regulate oncogenes in sequence-specific manner. However, systemic delivery of RNAi to tumors encounters myriad obstructions, and strategies to overcome such barriers have largely consisted of academic demonstrations with few approaches reaching patients. Here we report the development of a self-agglomerating nanohydrogel (SANGs) platform that selectively localizes to tumor tissue, is efficiently internalized by cancer cells, is agnostic to RNAi payload, and achieves functional suppression of multiple oncogene targets. After intravenous injection, SANGs preferentially accumulate and are retained in primary and metastatic loci in four aggressive cancer models in rodents. SANGs deliver multiple RNAi payloads that significantly suppress oncogene expression and sensitize previously resistant tumors while being safe and well tolerated in simulated clinical applications across three species. We propose, and provide the first direct evidence in support of, a mechanism featuring emergent material properties by which SANGs achieve durable solid-tumor delivery without attachment of cell- or tumor-targeting ligands. Overall, the SANGs platform is an enabling technology for RNAi-based cancer therapeutics and is poised for advanced pharmaceutical development with multiple solid-tumor indications.

RNA interference (RNAi) uses small interfering RNA (siRNA) and microRNA (miRNA) to silence the expression of target genes in a sequence-specific manner[1,2]. RNAi molecules hold unique potential as clinically viable modalities for manifold diseases[3,4]. Oncological indications are of particular interest because the vast majority of cancer-promoting genes are "undruggable"[4]. In order to reach its potential, RNAi molecules must be delivered to tumors, preferably after systemic injection. However, successful delivery of oligonucleotides is challenging due to their rapid clearance, nuclease susceptibility, and inability to traverse plasma membranes, resulting in insufficient localization to, and inadequate penetration of, tumors[5–7].

Numerous strategies have been developed to overcome these barriers, notably by incorporation of siRNA into lipid nanoparticles (LNPs), cationic polymers, or by chemical modification[7–12]. While these

[1]School of Biological Sciences, Georgia Institute of Technology, Atlanta, GA, USA. [2]Parker H. Petit Institute for Bioengineering and Bioscience, Georgia Institute of Technology, Atlanta, GA, USA. [3]Discovery and Developmental Therapeutics Research Program, Winship Cancer Institute, Emory University School of Medicine, Atlanta, GA, USA. [4]Bioengineering, Georgia Institute of Technology, Atlanta, GA, USA. [5]George W. Woodruff School of Mechanical Engineering, Georgia Institute of Technology, Atlanta, GA, USA. [6]School of Chemical and Biomolecular Engineering, Georgia Institute of Technology, Atlanta, GA, USA. [7]Wallace H. Coulter Department of Biomedical Engineering, Georgia Institute of Technology and Emory University School of Medicine, Atlanta, GA, USA. [8]School of Chemistry and Biochemistry, Georgia Institute of Technology, Atlanta, GA, USA. [9]Robert P. Apkarian Integrated Electron Microscopy Core, Emory University, Atlanta, GA, USA. ✉e-mail: nickhousley@gatech.edu

strategies have improved delivery, trafficking is poorly understood[13] and adequate design rules do not yet exist[14–17]. For example, LNP doses often become trapped in the liver and are not efficiently taken up by cancerous cells after systemic injection[18–20]. This leaves the majority of cancers untreated, especially metastases[18]. Cationic polymers face different challenges: they bind nonspecifically to many cell types[21,22] and interact with serum components, resulting in short circulation times and toxic side effects[23,24]. Surface modifications can improve stability, reduce nonspecific binding and clearance, and prolong circulation, but can also diminish target cell uptake[25–28]. While ligand functionalization can improve specificity, it increases manufacturing complexity and costs, reduces stability, and requires prior knowledge of the cell type of interest[18,19,29]. Carrier-free delivery of siRNA can be achieved through chemical modification, which drastically improves in vivo stability. While this has led to several FDA-approved drugs, none have oncological indications[7]. Collectively, the development of a systemic, tumor-agnostic delivery system that is effective, safe, and simple to manufacture remains an important missing link for therapeutic translation of RNAi.

Here, we report the development of self-agglomerating nanohydrogels (SANGs) as a platform that achieves durable solid-tumor delivery without direct functionalization with targeting ligands. We demonstrate that SANGs enable efficient delivery of RNAi molecules in vitro and exhibit preferential accumulation and retention in primary and metastatic loci in four cancer models in a species-agnostic manner, sensitizing previously drug-resistant tumors. SANGs were found to be safe and well-tolerated in simulated clinical applications across three species. We provide a provisional mechanistic proposal to explain how SANGs operate, which takes advantage of an emergent property of these materials in vivo. Finally, we provide the first direct observation of this emergent material property under biologically relevant conditions.

Results

SANGs synthesis and characterization

Poly(methacrylamide)-based core-shell nanohydrogels are formulated as soft and biocompatible particles using a simple, two-stage free-radical precipitation polymerization method first described by Lyon and coworkers (Fig. 1a, Supplementary Fig. 1)[30–32]. We previously observed that nanohydrogels functionalized with tumor-targeting peptides exclusively targeted ovarian tumors[33]. However, instead of functionalizing the shell layer with directing ligands, we explored the capabilities of untargeted nanohydrogels (SANGs), chemically functionalized only by the attachment of a small amount of fluorophore by amide bond formation. Physicochemical properties were characterized (Fig. 1b, c, Supplementary Fig. 1) and independently validated by the Nanotechnology Characterization Laboratory under conditions involving different solvents, dilutions, and temperatures (Fig. 1d, Supplementary Fig. 2).

Loading of siRNA molecules into these materials is performed by swelling lyophilized particles in RNA-containing buffer. SANGs do not contain a large amount of amine groups, as APMA (the amine-containing monomer) is introduced only in the shell, and only at 0.5% of the total monomer concentration during that step. Thus, oligonucleotides are unlikely to be retained by strong charge complementarity with cationic groups on the component polymer: the N:P ratio of effective siRNA-carrying SANGs particles is only approximately 0.24. Indeed, labeling of the SANGs with a large excess of dye NHS ester reagent (and therefore acylating most or all of the available amine groups) induces little or no change in siRNA carrying or delivery properties. We have not characterized the spatial distribution of RNA cargo within the core-shell structure, but given the modest change in measured zeta potential after siRNA loading (Supplementary Fig. 1), RNA is likely internalized and not surface-bound or at the core-shell interface. The observed stability of siRNA function in complete media and after pretreatment with RNase (0.03 mM) prior to transfection further supports an internalized distribution of siRNA, which would be expected to shield the cargo from the full complement of ribonucleases in FBS supplements (Supplementary Figs. 2, 9). After removal of unencapsulated siRNA, release follows a two-stage process with much of the cargo remaining entrained in the particles for extended periods[30]. Both siRNA-loaded and unloaded SANGs were found to be unchanged in size, morphology, and concentration upon storage at −25 °C, 4 °C, and 25 °C out to 60 days in aqueous conditions (Fig. 1e). SANGs prepared with negative control (NC) and scrambled RNAi molecules were shown to have no significant effect on the viability of HEY-A8-F8 cells (75 nM in particles, Fig. 1f).

SANGs undergo endosomal uptake and escape

SANGs were taken up readily by HEY-A8-F8 cells in dose- and time-dependent fashion (Fig. 1g, h, Supplementary Fig. 3) in standard cell culture media (10% FBS) and elevated (50% and 90% FBS) serum concentrations simulating physiological conditions (Supplementary Fig. 2). Application of SANGs for increasing lengths of time (ranging from 30 min to 24 h) revealed detectable intracellular uptake by 1 h, which increased until maximal fluorescent signals were reached at 18 h (Supplementary Fig. 3). Internalization was comparable for epithelial (OVCAR3) and mesenchymal (HEY-A8-F8) type ovarian cancer cells, as well as MCF7 breast cancer cells (Supplementary Fig. 4). Internalized SANGs remained unchanged in terms of cellular localization and fluorescence intensity for at least 24 h (Supplementary Figs. 3, 4). SANG cellular uptake was shown to be energy-, clathrin-, and macropinocytotic-dependent (Fig. 2a–c, Supplementary Fig. 5) and unperturbed by inhibition of caveolar mechanisms (Supplementary Fig. 5), suggesting a combination of clathrin-mediated endosomal and macropinocytotic pathways. This conclusion was further corroborated by live-cell imaging with an endosomal marker (wheat germ agglutinin, WGA)[34,35]) and SANGs containing dye-labeled siRNA, showing simultaneous co-localization of all components in HEY-A8-F8 cells at early time points up to six hours (Fig. 2h, Supplementary Fig. 6). After 18 h, however, siRNA and SANGs were observed to be distributed throughout the cytoplasm (Fig. 2d-f, Supplementary Figs. 2, 6, 7, and Supplementary Movies 1, 2), with low correlation ($R = 0.142 \pm 0.16$, $n = 24$) between siRNA and endosomes, whereas no siRNA signals were detected in siRNA-only experiments (Supplementary Fig. 8). These data suggest an efficient process of endosomal escape and release from the particles (Fig. 2g, Supplementary Movie 3).

Blockade of epidermal growth factor receptor (EGFR) kinase activity has been used for cancer therapy. However, other kinase-independent functions of EGFR also mediate pro-survival and chemoresistance, so siRNA-mediated knockdown should be able to achieve levels of therapeutic efficacy inaccessible to kinase inhibition alone. Consistent with the apparent escape of siRNA to the cytosol, efficient suppression of *EGFR* mRNA and protein (Supplementary Fig. 9) was observed in overexpressing HEY-A8-F8 cells after treatment with SANGs formulated with siRNA (20 nM) against *EGFR* and (separately) against *KRAS,* resulted in significant mRNA knockdown, in each case to a degree similar to that observed using the same concentration of siRNA delivered with lipofectamine (Fig. 2i). The same formulation substituting the miRNA-429 induced phenotypic epithelial-to-mesenchymal transition and target mRNA (*ZEB1*) suppression. SANGs containing scrambled siRNA had no effect (Supplementary Fig. 9).

SANG biodistribution and retention in mouse and rat

The in vivo biodistribution of SANGs was explored with xenograft and orthotopic murine models of ovarian and breast cancer and a genetically-engineered rat model of colorectal cancer to survey different tumor types, induction methods, and species, all in the context of a functioning immune system. Each of the cancer strains employed

https://doi.org/10.1038/s41467-025-66788-4

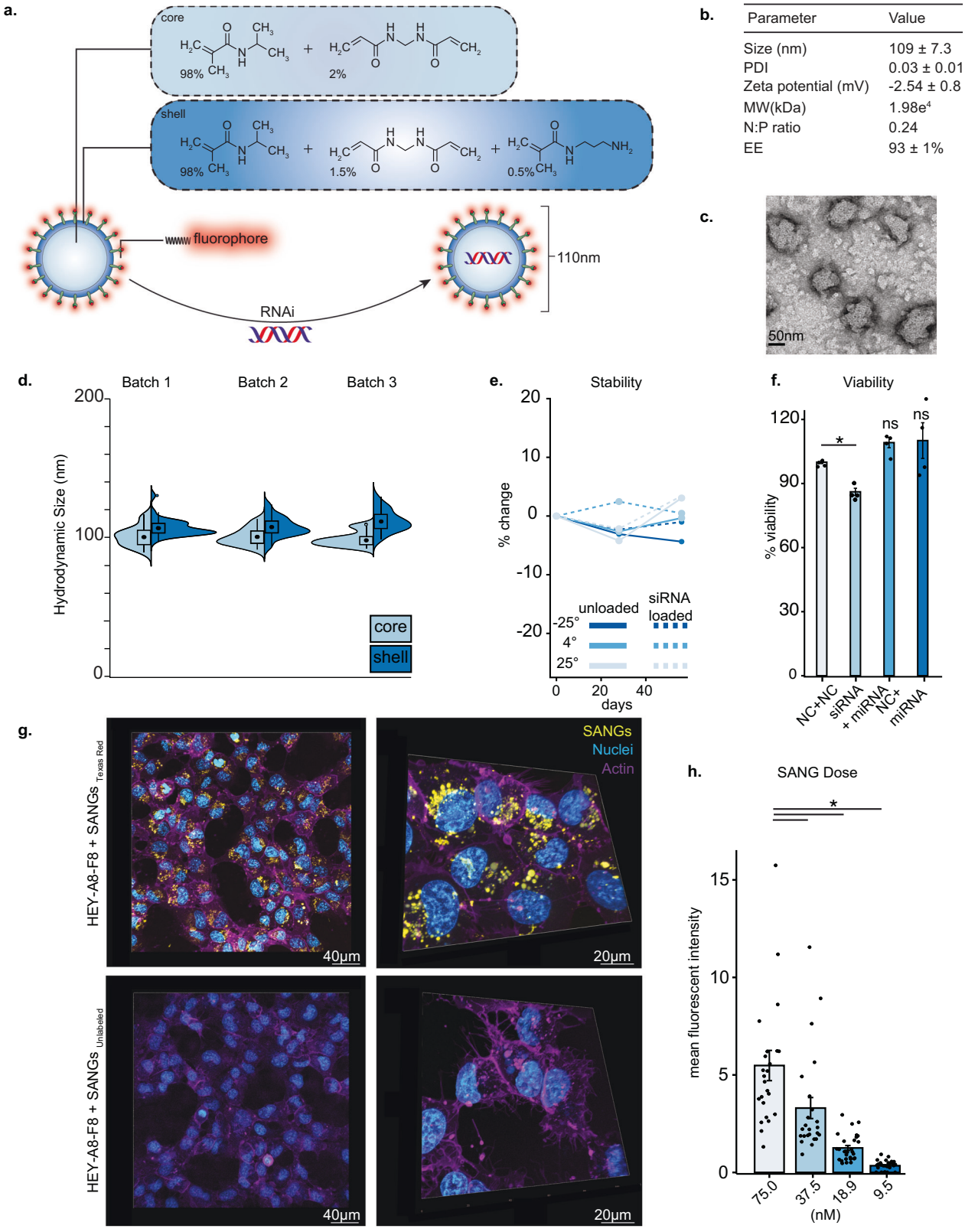

was engineered to express luciferase and thus could be readily followed by bioluminescence imaging (BLI).

Within 30 min following i.v. injection in murine ovarian and breast cancer models, SANGs accumulated in regions with higher BLI signal indicating presumptive tumoral localization (Fig. 3a, Supplementary Fig. 10). In vivo distribution of SANGs was distinct from unloaded siRNA and free dyes, which were detected in regions devoid of BLI signal in lungs (within 5 min) and in liver shortly thereafter (30 min) (Fig. 3a). By 24 h, the specificity of biodistribution improved out to 72 h (Fig. 3b) where little (if any) SANGs were detected outside BLI inferred tumors. The in vivo biodistribution and siRNA delivery of SANGs was equivalent to that previously observed for targeted (YSA-functionalized) nanohydrogels[33] and repeated in Supplementary Fig. 11, indicating that the targeting ligand is irrelevant. SANGs remained closely

Fig. 1 | Physicochemical property characterization of SANG and its cellular uptake. a A schematic representation of the synthesis and composition of fluorescently labeled siRNA-loaded SANGs. **b** Physicochemical property characterization of SANGs, including the hydrodynamic diameter (Wyatt DLS), polydispersion index (PDI–Wyatt DLS), zeta potential, molecular weight (MW), N:P ratio, and encapsulation efficiency (E.E.). **c** Negative-stain TEM image of SANGs. **d** Reproducibility of SANG production across 3 independent batches ($n = 30$ independent measures/batch for each core and shell) showing the complete size distribution of the core and shell components prior to final cleaning and purification. **e** Chemical stability of siRNA-loaded and unloaded SANGs at −25 °C, 4 °C and 25 °C (mean of $n = 3$ independent batches per condition. **f** Cell viabilities (Hey-A8-F8) of SANGs (75 nM) differentially loaded with negative control (NC) siRNA-*EGFR* (siRNA) and mir-429 (miRNA), normalized to saline-treated cells ($n = 4$ independent experiments). **g** Cellular uptake in Hey-A8-F8 ovarian cancer cells following overnight incubation (18 h) with Texas-Red labeled (top) and unlabeled (bottom, to rule out the possibility of autofluorescence artifacts) SANGs (yellow pseudo-colored for contrast) for both low (left, 20x) and high (right, 63x) magnification views. Cells (purple) visualized with Lectin DyLight™ 649 (Vector Laboratories). **h** Semi-quantitative analysis of the dose-dependent mean fluorescent intensity (MFI) measured in Hey-A8-F8 cells 18 h following incubation of Texas-Red labeled SANGs. Data points derived from confocal images acquired under identical conditions. Barplots present data as mean ± se as well as all data points. (*) indicates statistically significant differences between experimental groups as empirically derived from a hierarchical Bayesian model. NS, Not significant.

associated with BLI signals 7 days after i.v. delivery, indicating preferential retention in tumors (Fig. 3c).

Analysis of excised tissues confirmed SANGs rapidly reached tumors, reaching 5.1 ± 1.2-fold increase by 4 h and a maximum (approximately 200-fold above background) at 72 h (Fig. 3c, Supplementary Fig. 12). While significantly reduced compared to peak, we find SANGs were retained in primary tumors 7 days after systemic delivery (Fig. 3c). In contrast, intravenous infusion of free siRNA (20 μM) gave significantly lower tumor localization at 3 and 7 days (1.14 ± 0.02 and 2.29 ± 0.17 fold above background, Fig. 3c)[36]. Quantitative analysis of SANG biodistribution to major organ systems confirmed that non-cancerous organs remained largely devoid of SANG signal out to one week, with the exception of a transient increase detected in the kidney (Fig. 3d, Supplementary Fig. 12b).

To test the metastatic localization capacity of SANGs, a limitation of existing RNAi delivery platforms[37], we modeled late-stage ovarian cancer by IP administration of HEY-A8-F8 cells. After confirming tumor induction and extensive abdominal metastasis, we administered SANGs intravenously and quantified biodistribution as described above. We observed expansive tumor load across the spleen, GI-tract, liver (Fig. 3e, f), and occasionally epidural metastasis (Supplementary Fig. 13), and corresponding rapid (4 h) and highly specific accumulation of SANGs in diffuse metastatic lesions (Fig. 3e). The temporal biodistribution in metastatic loci closely mirrored that of primary tumors, independent of organ (Fig. 3g), while signal in the non-cancerous portions of organs remained largely devoid of SANG signal (Fig. 3d–f, Supplementary Figs. 12, 14).

Co-localization analysis of ex vivo SANG fluorescence and tumor bioluminescence (Fig. 3h) showed a strong association between SANGs and diffuse metastases ($R = 0.84$, $p < 0.001$, Supplementary Fig. 14) with >96% of the SANG signal residing within 15% of the line of identity. Few if any (< 0.1%) metastatic loci were untargeted by SANGs (below line of identity) while only 3.5% of SANGs were detected in regions without any BLI confirmed metastasis. These results indicate a low level of off-target accumulation and corroborate biodistribution data observed in less metastatic murine models. Taken together, these results indicate that SANGs rapidly localize to both primary and metastatic murine tumors, are retained for extended periods of time, and have minimal off-target accumulation (Fig. 3d).

To quantitatively assess SANGs biodistribution in off-target tissues, we compared the cellular distribution of SANGs to that of a well-documented liver-targeting LNP formulation based on the lipid LP01 (Fig. 3i)[38]. In separate cohorts of control (C57BL/6) mice, we intravenously injected SANGs or LNP-LP01 ($n = 4$ and $n = 3$ independent biological replicates, respectively), each formulated to carry AlexaFluor-647 labeled siRNA against *EGFR*. After three hours, $CD31^{-}CD45^{-}$ (epithelial and stromal), $CD31^{+}CD45^{-}$ (endothelial), and $CD31^{-}CD45^{+}$ (leukocyte) cell populations were isolated from liver and kidney, and the number of those cells carrying the AlexaFluor dye was quantitatively determined. As expected, significantly more cells extracted from liver in LNP-LP01 treated animals were dye labeled compared to PBS (1X, pH 7.4) controls (Fig. 3j). With the exception of presumptive renal endothelial cells, significantly more $CD31^{-}/CD45^{+}$ and $CD31^{-}/CD45^{-}$ cells extracted from kidneys also were labeled with the dye, presumably by LNP uptake (Fig. 3h). In contrast, we found only 4% of $CD31^{-}/CD45^{-}$ renal cells from SANGs treated animals to contain significant amounts of dye relative to PBS (1X pH 7.4) treated controls (Fig. 3j). Collectively, across all cell-types studied, we found 10–30 times fewer dye-labeled cells in SANGs treated animals compared to LNPs (Supplementary Fig. 15), thereby verifying whole organ and confocal microscopy biodistribution data (Supplementary Fig. 15). Ovarian tumor bearing mice were intravenously injected simultaneously with LNP-LP01 formulated to carry AlexaFluor-647 labeled siRNA against *EGFR* and SANGs formulated to carry Texas-Red labeled siRNA against *EGFR*. Analysis of excised tissues at one and four hours after injection demonstrates orthogonal biodistribution between SANGs and LNP-LP01 (Supplementary Fig. 15).

Intravenous delivery of SANGs to rats genetically engineered to spontaneously develop colorectal cancer resulted in immediate diffuse SANG signal across the abdominal cavity which began to coalesce in small punctate intensities around the perimeter of the abdomen, suggestive of preferential distribution to the diffuse tumors (Fig. 4a, Supplementary Fig. 16). SANG distribution remained localized in this fashion for 7-days with increasing signal-to-noise ratio over time, indicating preferential tumor retention. In contrast, free siRNA distributed mostly to the liver followed by elimination (Fig. 4a). Ex vivo analysis of colon with diffuse adenocarcinomas (Fig. 4b) showed detectable SANG signal at 4 h, increased signal at 24 and 48 h, and a maximal recorded value at 7 days (Fig. 4c); mouse biodistribution peaked at 72 h (Fig. 3c). As in mouse, SANGs remained largely absent from other major rat organs with the exception of a nominal increase detected in liver and in the kidney (Fig. 4c) which was confirmed by confocal microscopy (Fig. 4d). Intravenous delivery of SANGs ($1\ mg{\bullet}kg^{-1}$) to lung tumor (GFP-MDA-MB-231) and non-tumor-bearing SRG rats showed significantly higher SANG delivery to tumor-bearing animals (Fig. 4e). SANGs tumor biodistribution progressively increase over time (Fig. 4f), consistent with in vivo behavior in mice with ovarian cancer and rats with colorectal cancer and correlated with tumor fluorescent intensity, a proxy for tumor load (Fig. 4g, h).

In vivo pharmacokinetics and clearance studies revealed an apparent bi-exponential blood distribution half-life (α) of approximately 2.5 h for SANGs and an elimination half-life (β) of ~13.4 h (Supplementary Fig. 17) in rats. While this value is comparable to that of other nanoparticle formulations[36,39], SANGs behave differently in at least one important respect. We found relatively high SANG concentrations in blood at 24 and 48 h, with between 2.8–5.6% of the initial dose remaining in circulation, a factor that likely played a role in the favorable tumor biodistribution and retention. Analysis of urine and feces showed rapid and near complete (~92%) excretion of naked siRNA by 24 h, which was dominated by renal metabolism, whereas only 16% of the SANG dose was excreted during the first 24 h. These data show that a large fraction of SANGs leaves systemic circulation

https://doi.org/10.1038/s41467-025-66788-4

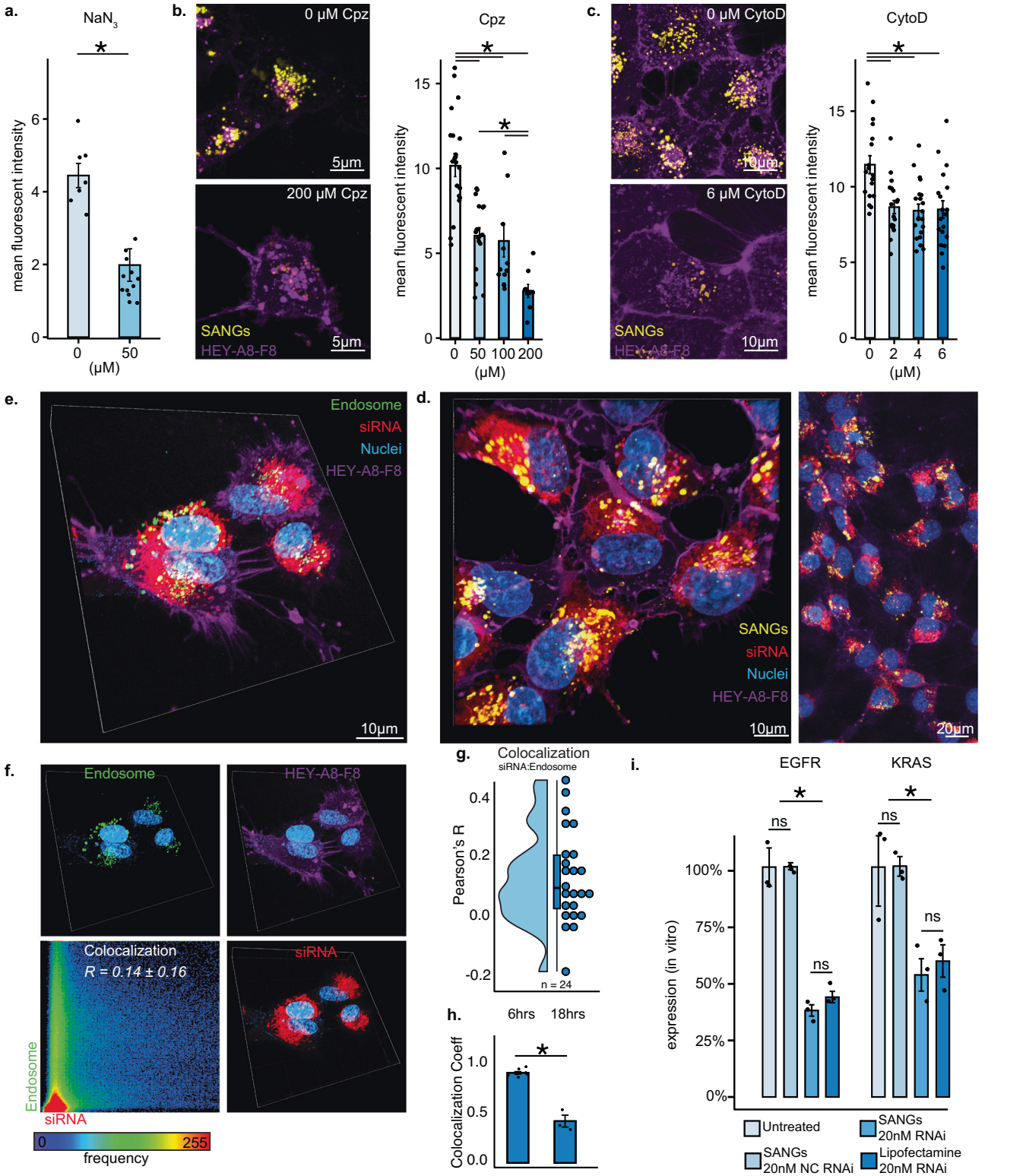

rapidly, partitions efficiently to tumors, and perhaps is also sequestered in low concentrations in tissues such as fat, to be released over time.

In vivo functionality of SANGs

When examined by confocal fluorescence microscopy, SANGs were found distributed throughout ovarian carcinoma (HEY-A8-F8) tumor sections and deep within tumor parenchyma, exhibiting an extravasated distribution into the tumor interstitium (Fig. 5c, Supplementary Fig. 18). A similar result was observed in mice with orthotopically implanted ovarian carcinomas (HEY-A8-F8) and breast cancers (MDA-MB-231) (Supplementary Figs. 10, 11) as well as in rats with advanced colorectal cancer, where we saw strong co-localization with EGFR-overexpressing tumor cells (Supplementary Fig. 18). In all cases, the extravasated distribution was retained for at least 7 days.

Across murine ovarian (HEY-A8-F8) and rat colorectal cancers, we found that a single intravenous infusion of SANGs loaded with siRNA against *EGFR* or *KRAS* resulted in dose-dependent reduction in mRNA

Fig. 2 | Mechanism of internalization, endosomal escape, and delivery of RNAi payloads. a Sodium azide (NaN_3) dependent reduction (18-h) of uptake of Texas Red-labeled SANGs (75 nM) by HEY-A8-F8 cells (AlexaFluor® 647 Phalloidin) as measured by mean fluorescence intensity. **b** Confocal fluorescence images (maximum intensity projections) following clathrin-mediated endocytosis inhibitor (chlorpromazine [Cpz]) and quantification of intracellular SANGs (75 nM) by HEY-A8-F8 cells following exposure to different doses of Cpz (18-h). **c** Confocal fluorescence images (maximum intensity projections) following macropinocytosis inhibitor (cytochalasin D [CytoD]) and quantification of intracellular SANGs following exposure to different doses of CytoD. SANGs were transfected at a final concentration of 75 nM. **d** Maximum intensity projections from z-stack (10 μm) confocal images of Hey-A8-F8 cells 18 h following incubation with Cy3-siRNA-loaded SANGs (AlexaFluor 488) at both low (right, 20x) and high (left, 63x) magnifications, showing intracellular distribution ($n = 3$ biological replicates). **e** Three-dimensional rendering of confocal images, dual-labeling endosomes (CellLight™ Endosomes-GFP) and siRNA (Cy3) 18 h following Hey-A8-F8 incubation with siRNA-loaded SANGs. **f** Individual fluorescent channels shown for clarity. ((**f**), lower left) Results of colocalization analysis performed on a pixel-by-pixel basis between endosomes and siRNA channels, where every pixel is plotted based on its intensity level. Scatterplot colors represent pixel density. **g** Quantitative results of colocalization analysis are summarized by the Pearson's correlation coefficients (R) between endosomes and siRNA. $n = 24$ cellular replicates. **h** siRNA release from SANGs quantified by colocalization coefficients (mean ± sd) between SANGs loaded with Cy3-labeled siRNA at 6 and 18 h after incubation with Hey-A8-F8 cells, $n = 24$ cellular replicates. SANGs were transfected at a final particle concentration of 75 nM particle concentration. **i** Down-regulation of *EGFR* and *KRAS* mRNA levels as quantified by RT-qPCR. The relative level of mRNA expression was calculated compared to NC siRNA controls and relative to lipofectamine-transfected siRNA. $n = 3$ biological replicates. Barplots present data as mean ± se as well as all data points. (*) indicates statistically significant differences between experimental groups as empirically derived from a hierarchical Bayesian model (stan_glm): 95% highest density intervals do not overlap between groupwise contrasts.

(Fig. 5a, b) and protein expression (Fig. 5c–e) in tumor tissue. Therapeutic efficacy of SANGs was then tested in mice with tumors established from HEY-A8-F8 ovarian carcinoma cells in a single-dose efficacy study. Enhanced expression of *EGFR* by these cells is correlated with drug resistance, and is a well-established model[40,41]. We treated groups of mice with two independent doses of SANGs, 24 h apart, the first loaded with mir-429 and the second with siRNA against *EGFR*, because mir-429-driven EMT reversal requires time to induce the necessary phenotypic change. Intraperitoneal cisplatin was then delivered 24 h later. Cisplatin alone was used as the standard of care control. All animals were euthanized six days after treatment to measure tumor size. Improvements relative to drug alone were evident from significant inhibition of tumor growth and reduction in tumor weight (Supplementary Fig. 18). These data indicate that SANGs successfully extravasate, penetrate tumor microenvironments, gain access to the specific cells of interest in a species- and tumor-agnostic manner, and sensitize previously resistant tumors in vivo.

Systemic delivery of SANGs is minimally toxic

A variety of tests revealed no significant toxicity associated with high doses (40x anticipated starting human dose) of either empty or scrambled miRNA/siRNA-loaded SANGs. These included observations with outbred mice and NOD-SCID mice with ovarian tumors including delivery of cisplatin (Supplementary Fig. 19). A repeat-dose tolerability study of high-dose SANG-siRNA and co-infused oxaliplatin in rats with advanced colorectal cancer[42] produced no mortality or any clinical signs of distress while weights recovered back to baseline by study completion (Supplementary Fig. 20). A maximal tolerable dose study in rats revealed only minor changes in blood chemistry at 6 and 24 h (Supplementary Fig. 20) and no difference from controls in histopathology of major organs for the three escalating doses (Supplementary Fig. 20 up to 96x anticipated starting human dose). Finally, a single acute dose study in an adult female (73 kg) Yucatan swine showed no clinically meaningful deviances out to 6 h following i.v. infusion of SANGs-siRNA at the same high dose (7 mg•kg^{-1}) with the exception of a transient increase in AST at 5 min (Supplementary Fig. 20). Thus, SANGs induce minimal, if any, toxicity in a variety of animals and experimental conditions. Taken together, these data establish a wide preliminary safety profile and strongly support the systemic use of SANG to deliver RNAi to solid tumor cancers.

Cancer specific delivery achieved through emergent self-agglomerating mechanism

The results described here set SANGs apart from most nanoparticulate delivery vehicles, their most striking property being selective homing to tumors without the use of designed ligands for cell-surface markers. Five complimentary methods were used to probe the mechanism(s) responsible for this in vivo performance. We sought to distinguish between mechanisms involving cell binding vs. physical properties of the particles that may promote selective distribution to tumor tissue. First, TEM was used to measure the size and number of SANG particles over concentrations ranging from 25.5 nM to 1.6 μM (Fig. 6a, b), which revealed an interesting dynamic behavior. At the lowest three concentrations studied, the number and size distribution of SANGs closely matched the values predicted by a linear dependence of concentration on the number of particles, expected for any solute that does not undergo changes in form with changes in concentration (Fig. 6b). At higher SANG concentrations, however, progressively smaller numbers of SANG particles were observed, with increasing sizes and size distributions (Fig. 6b, Supplementary Fig. 21). High magnification views showed different representative forms of tightly clustered SANGs that emerged above 156 nM. Similarly, aqueous dynamic light scattering (DLS) on two different instruments showed strongly monodispersed hydrodynamic size distributions at low concentration (52 nM), but clear evidence of larger and less regular aggregates at 156 nM (Fig. 6c, Supplementary Fig. 21). When concentrated SANGs samples were re-diluted, much of the material returned to the original size range on average as indicated with DLS (Supplementary Fig. 21) while larger aggregated states were detected with TEM (Fig. 6a).

Parallel diffusion-ordered NMR measurements allowed us to detect diffusional changes caused by aggregation. A significant decrease in diffusion coefficient (21.5%) and T2 relaxation time was observed over a 10-fold range of SANG concentration (Fig. 6d, Supplementary Fig. 22). The former parameter indicates slower particle movement in solution, and the latter reflects restricted molecular motion[43–45], both consistent with nanogel agglomeration in solution. This phenomenon was directly visualized by liquid-phase transmission electron microscopy (LP-TEM), allowing us to directly measure SANG behavior with nanometer-scale and sub-second resolution in a liquid environment. Liquid cell chambers with 150 nm apertures were used to provide adequate room for particle motion. SANGs were readily detected above background and demonstrated clear evidence of nanogel agglomeration throughout every field of view studied. SANGs were observed to 'snap' together in long chains and islands similar to structures observed with negative stain TEM (Fig. 6a), much larger and less mobile at higher concentration and retaining their close association as they rotated across the fields of view (Fig. 6e, Supplementary Movie 4). This real-time, nanoscale evidence of nanogel agglomeration in naturalistic conditions provides the first direct observations of the emergent SANG materials property.

To test if nanogel aggregation occurs in vivo, we sequentially intravenously infused two populations of SANGs conjugated to different fluorophores in rats with advanced colorectal cancer. If SANGs do not agglomerate in vivo (and if not every cell is flooded with particles), fluorescent signals from both populations would co-localize at a nominal frequency determined by chance. Conversely,

https://doi.org/10.1038/s41467-025-66788-4

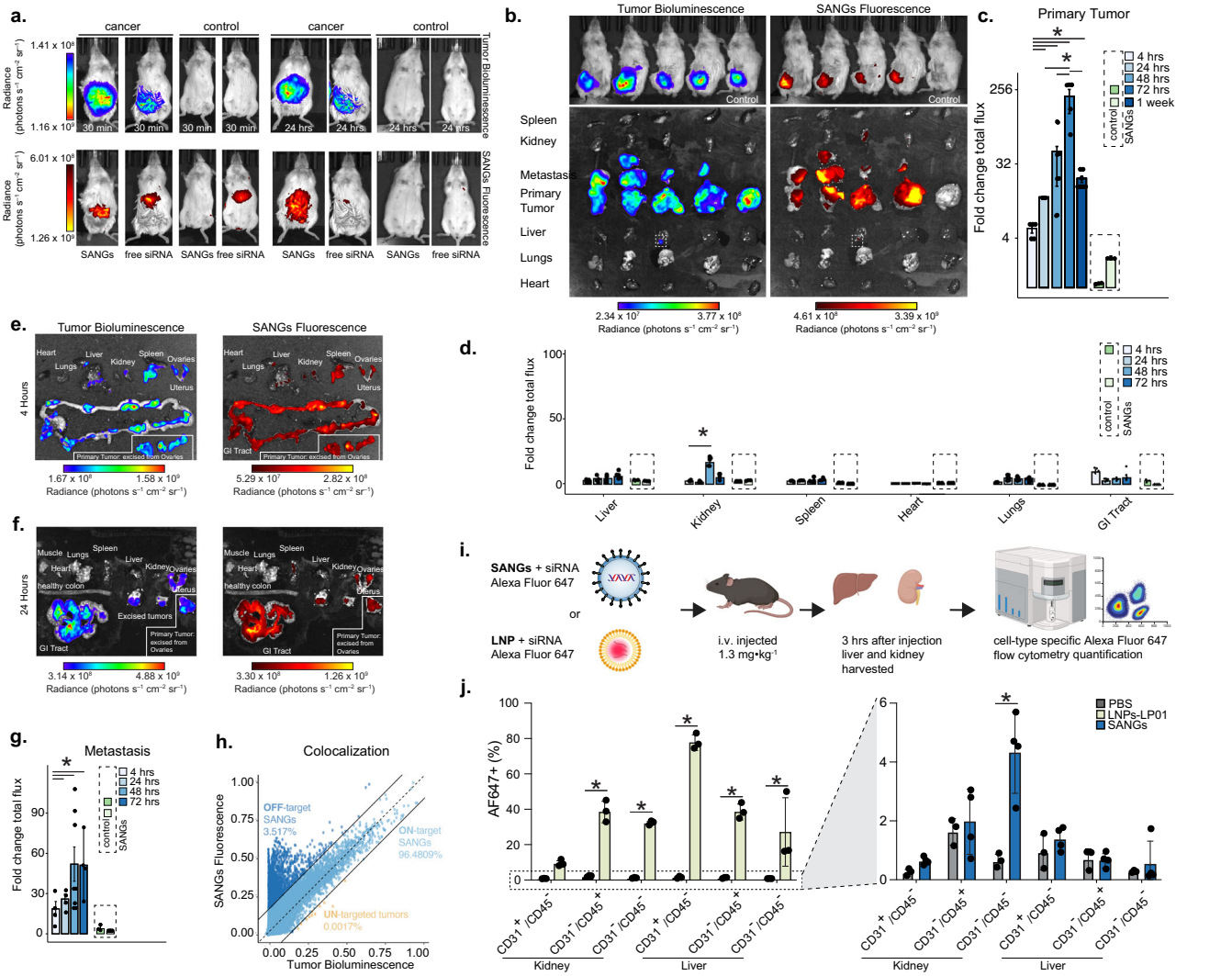

Fig. 3 | Preferential biodistribution in primary and metastatic tumors and comparison with LNP. a Whole-body imaging of mice after intravenous injection of free siRNA (Cy3-labeled, 16 μg labeled siRNA) or Texas Red-labeled SANGs (1 mg•kg^{-1}, carrying 16 μg unlabeled siRNA). Tumor bioluminescence and SANGs fluorescence were imaged sequentially in ovarian cancer-bearing and control mice, showing distribution at 30 min and 24 h after i.v. injection. **b** Whole-body imaging of ovarian cancer-bearing mice 72 h after intravenous injection of SANGs (1 mg•kg^{-1}) or saline control. Ex vivo imaging of tumors and major organs was immediately imaged after in vivo imaging was completed. **c** Quantification of SANG delivery and retention to ovarian tumors. **d** Quantification of SANG delivery and retention across specified time points across all major organ systems, free siRNA (Cy3-labeled) used as control ($n = 4–5$ biological replicates). **e**, **f** Representative ex vivo images at 4 and 24 h after intravenous injection of SANGs (1 mg•kg^{-1}) to mice following metastatic tumor induction. **g** Quantification of SANG delivery and retention to metastatic ovarian tumors, free siRNA (Cy3-labeled) used as quantitative control ($n = 4$-8 biological replicates). **h** Colocalization analysis of ex vivo SANG fluorescence and tumor bioluminescence. Dotted line of identity indicates perfect colocalization with ±15% bounding conditions. Signals above this ±15% bounding conditions indicate off-target SANGs, i.e., dye-labeled SANGs fluorescence signal without corresponding bioluminescence signal. Below this ±15% bounding conditions show untargeted cancer, i.e., bioluminescence without a corresponding SANGs signal. **i** illustration of the study to compare SANG and LNP biodistribution created with BioRender. **j** Determination by flow cytometry of the efficiency of AlexaFluor-647 labeled siRNA against *EGFR* to CD31^{-}CD45^{-}, CD31^{+}CD45^{-}, and CD31^{-}CD45 cell populations from liver and kidneys by LNP-LP01 ($n = 3$ biologically independent experiments) and SANGs ($n = 4$ biologically independent experiments) relative to PBS (1X pH 7.4) control ($n = 3$). All SANG fluorescence data were acquired with Texas Red-labeled particles. Barplots present data as mean ± se as well as all data points. (*) indicates statistically significant differences between experimental groups as empirically derived from a hierarchical Bayesian model (stan_glm): 95% highest density intervals do not overlap between groupwise contrasts.

co-localization to a greater degree would indicate that agglomeration does indeed occur prior to or during tissue/cell accumulation. Fluorescent signals from SANGS of both colors were readily detected (Fig. 6f, Supplementary Fig. 23) and found to be co-localized significantly more often than that expected by chance. Furthermore, colocalized deposits (both colors) were significantly larger (~ 74-fold) than non-colocalized (single color) SANGs (Supplementary Fig. 23). A very stable, non-aggregating comparator, the Qb virus-like particle (Qβ-VLP), was dye-labeled in the same manner (Supplementary Fig. 24) and was found in its expected location (liver)[46] with random co-localization frequency (Fig. 6g). Collectively, results from these five methodologically independent experiments are consistent with the hypothesis that environmentally-responsive aggregation is at least partially responsible for the preferential tumor delivering property of SANGs (Fig. 6h).

Characterization of SANGs biomolecular corona

Given the role that biomolecular coronas can play in biodistribution, we tested if protein coronas form on SANGs (Fig. 7a). Quantitative proteomic study of the protein corona of SANGs in rat serum

https://doi.org/10.1038/s41467-025-66788-4

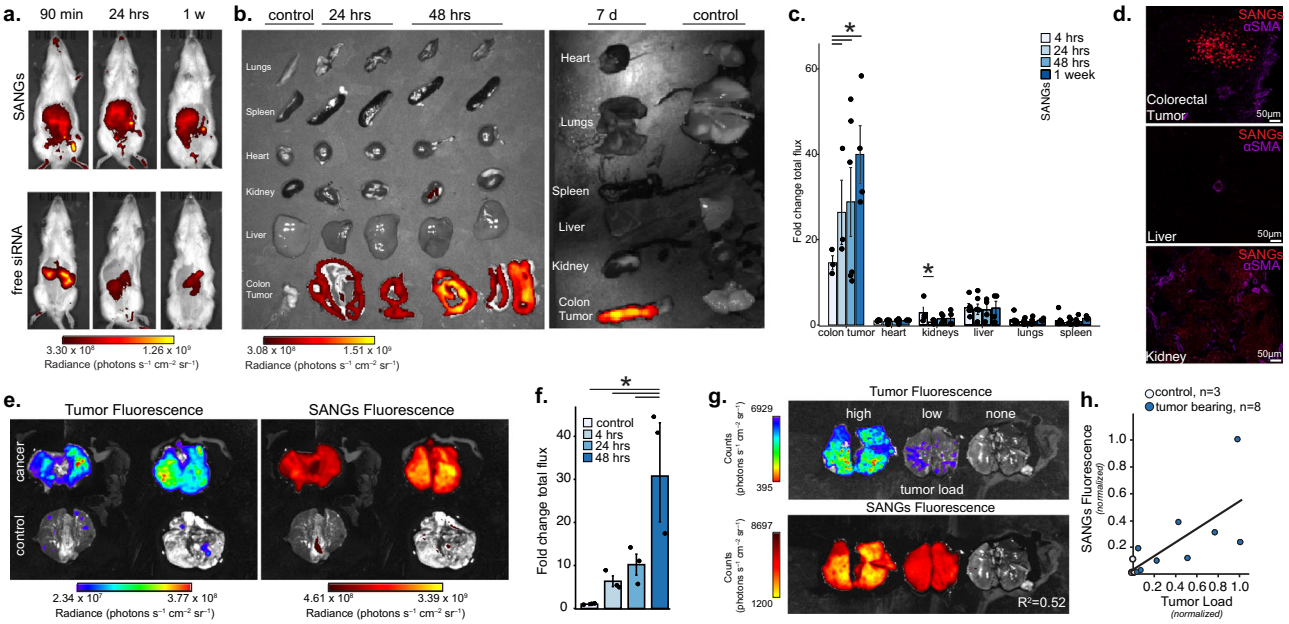

Fig. 4 | Tumor agnostic, cross species in vivo and ex vivo biodistribution. **a** Sequential whole-body imaging of Pirc rats after intravenous injection of free siRNA (Cy3-labeled) or Texas Red-labeled SANGs (1 mg•kg^{-1}) showing the immediate (90 min), early distribution (24 h), and retention (1 week). **b** Ex vivo imaging of tumors and major organs. **c** Quantification of the specificity of SANG delivery and retention to tumors and major organs (liver, kidney, spleen, heart, lungs), normalized against SANG fluorescence signal in heart. Top inset shows the enlarged colorectal tumor biodistribution of SANGs across time. Representative color photograph of a section of the internal lumen of the descending colon of a Pirc rat, indicating diffuse adenocarcinomas ($n = 3$–6 biological replicates). **d** Confocal microscopy of SANG distribution in advanced colorectal cancer. Z-projections of confocal images dual-labeling vessels (anti-alpha smooth muscle actin) and SANGs, tumor, liver, and kidney extracted from an identical Pirc rat 72 h after intravenous injection of SANGs (1 mg•kg^{-1}, $n = 3$ biological replicates). **e** Ex vivo imaging of lungs from tumor-bearing and control SRG female rats 48 h after SANG dose (1 mg•kg^{-1}). **f** Quantification of the specificity of SANG delivery and retention to tumors normalized against SANG fluorescence signal in the heart. **g** Representative ex vivo images showing SANG delivery relative to differential tumor load and **h** quantification across all lung-tumor bearing SRG rats ($n = 8$) and control ($n = 3$). All SANGs fluorescence data were acquired with Texas Red-labeled particles. Barplots present data as mean ± se as well as all data points. (*) indicates statistically significant differences between experimental groups as empirically derived from a hierarchical Bayesian model (stan_glm): 95% highest density intervals do not overlap between groupwise contrasts.

compared to coronas formed on LP01 nanoparticles, a well-known drug delivery vehicle[38], revealed significant differences between the platforms. LP-01 coronas contained significantly more proteins, present in much greater abundance, than those associated with SANGs, which were present in amounts only marginally higher than background (nonspecifically bound proteins) (Fig. 7b). Figure 7c illustrates the distribution of distinguishing corona proteins detected after filtering out background plasma proteins (FDR < 0.001 and > 1.5-fold-change relative to plasma sample), with protein identities listed in Supplementary Data 1. Hierarchical clustering further emphasized the stark difference between LP01 and SANG protein coronas, showing shared abundances and compositions of only one of eight clusters containing 6 of 115 proteins (Fig. 7d, Supplementary Data 2). Thus, SANGs develop a significantly lessx dense (in number and abundance) and compositionally distinct protein corona relative to LP-01. Determining the role played by the protein corona on SANGs function will be the focus of future studies.

Discussion

Formulated to contain positively charged groups to facilitate the carrying of oligonucleotides, core-shell polyacrylamide-based SANGs were shown to efficiently package and stabilize RNAi molecules and to deliver siRNA and miRNA to three cancer models, equally well in both mouse and rat across primary and metastatic loci. The RNAi cargo successfully sensitized drug-resistant tumors, allowing subsequent delivery of chemotherapeutic agents to have a dramatically enhanced effect in arresting tumor growth in vivo. The nanogel platform was found to be minimally toxic and well-tolerated in mice, rats, and swine in a variety of simulated clinical applications. The most remarkable properties exhibited by SANGs are: 1) preferential delivery to primary and metastatic tumors[47] relative to healthy tissue upon systemic administration, 2) prolonged tumor retention, 3) extravasation into the tumor interstitium, gaining access to cancerous cells, and 4) delivery of sufficient RNAi payloads to silence oncogene mRNA and protein expression and result in efficient tumor growth suppression. While much is known about barriers to, and mechanisms for, tumor targeting and entry[37,48–50], we are unaware of a systemically administered delivery platform of any form—polymeric, liposomal, proteinacious, or viral—with this combination of advantages, including a large number of nanoparticles captured in a recent meta-analysis of biodistribution[51]. Excellent comparators include a layer-by-layer formulated polymer nanoparticle with outstanding ovarian cancer targeting ability after intraperitoneal, but not intravenous, delivery[27], and the delivery of siRNA to pancreatic tumors with high selectivity[52] using a system that self-assembles in vivo. (Here, the authors also consider the physical state of tumor tissue as a potential contributing factor to nanoparticle targeting, citing prior work focusing on nanoparticle size and shape.) An early contribution found differently-sized dextrans to partition into skin cancer tumors to a degree controlled by opposing factors of vascular permeability (favoring smaller dextrans) and circulation lifetime (favoring larger dextrans)[53]. We have found SANGs to be much more deformable than dextrans, in that the former pass through low-molecular-weight-cutoff size-exclusion filters, whereas the latter do not.

We currently propose that tumor accumulation and retention derive from an environmentally responsive “self-agglomeration” behavior demonstrated in vitro and in vivo. Fig. 5g summarizes the following provisional mechanistic hypothesis. When administered

https://doi.org/10.1038/s41467-025-66788-4

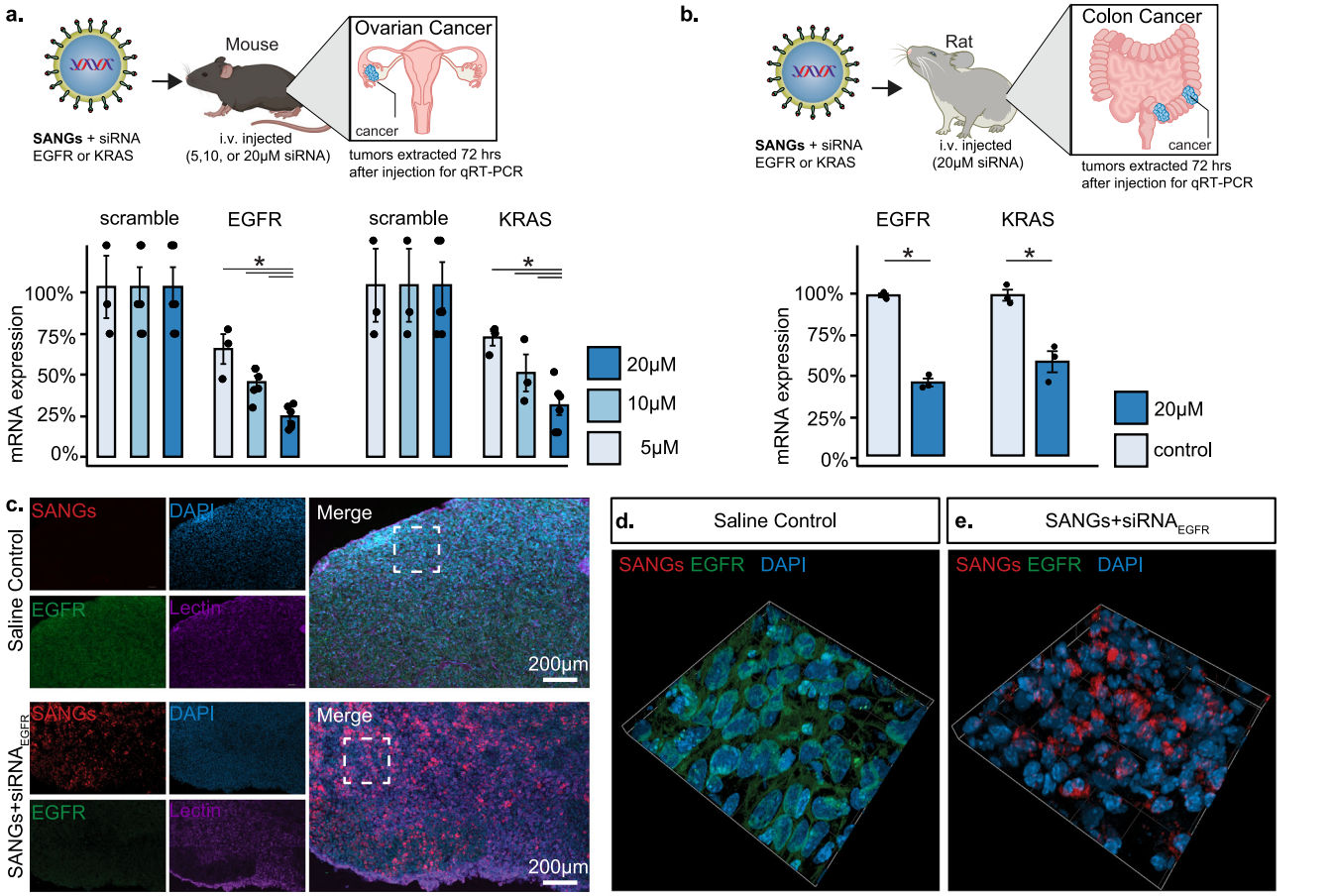

Fig. 5 | In vivo tumor penetration and efficacy. a Dose-dependent down-regulation of *EGFR* and *KRAS* mRNA levels as quantified by RT-qPCR ($n = 3$ independent experiments) in ovarian cancer-bearing mice following SANG-mediated delivery of siRNA against *EGFR* and *KRAS*, respectively. The relative level of mRNA expression was calculated over the scrambled siRNA control, each of which was normalized to GAPDH. **b** Down-regulation of *EGFR* and *KRAS* mRNA levels as quantified by RT-qPCR ($n = 3$ independent experiments) in Pirc rats. The relative level of mRNA expression was calculated over the scrambled siRNA control, each of which was normalized to RPS18. **c** representative 20x LSCM images of tumor sections (orthotopic Hey-A8-F8) from mice 48 h after intravenous administration of either negative control siRNA loaded Texas Red-labeled SANGs (top) or siRNA against *EGFR* loaded SANG (bottom), $n = 4$ biological replicates. **d**, **e** Three-dimensional (z-stack) confocal microscopic images show an expanded view (63x) of white dotted sections in (**c**). Intracellular distribution of endosomes and siRNA 18 h following Hey-A8-F8 incubation with SANGs loaded with Cy3-labeled siRNA. Merged images of cell nuclei (DAPI), EGFR (AlexaFluor 488) and SANGs (Texas Red). Barplots present data as mean ± se as well as all data points. (*) indicates statistically significant differences between experimental groups as empirically derived from a hierarchical Bayesian model (stan_glm): 95% highest density intervals do not overlap between groupwise contrasts. Schematics created with BioRender.

intravenously, SANGs distribute to all organs proportional to the perfusion rate. However, the elevated resistance, sluggish blood flow, and increased tortuosity overrepresented in the maladaptive vasculature of tumors[53–55] allow more time for SANGs particles to aggregate[56–58] in regions of slow flow or imposed shear forces or increase the collisional frequency of SANGs particles in regions of flow discontinuity, each of which is likely to stimulate self-agglomeration and entrainment in tumors. An analogy may be found in the pronounced tendency of blood clots to form at tubing junctions in extracorporeal blood circulation devices[58]. Furthermore, agglomeration is a nucleated process rather than a linear one. Once aggregates start to form, increased agglomeration is more and more likely. This is manifested in vitro by the threshold relationship between particle size and concentration. Agglomeration favors retention in the TME relative to other non-malignant capillary beds[53] and results in the de novo generation of SANG depots in tumor vessels. This progressive accumulation process is supported by the slow accumulation in SANGs up to 72 h after IV administration in mice and up to 1 week in rats. SANG depots are then the driving force for extravasation down a concentration gradient into the intestinal space which is likely due to both active and passive processes[13,59–62]. Once in the interstitial space (see Fig. 5a–c, f), SANGs enter cells via clathrin-mediated endocytosis and macropinocytosis. While we observe functional siRNA delivery, we do not yet know the mechanism by which SANGs escape endosomal/micropinocytotic entrapment, which will be the focus of future studies.

Because accumulation occurs with multiple tumor types in multiple species, we believe it is unlikely that a specific receptor-mediated process is responsible for cancer cell targeting, although we cannot fully rule out, for example, multivalent recognition of surface features of unfunctionalized SANGs. It is more likely that the emergent dynamic behavior of SANGs—the existence of which is supported by the self-consistent results of five complementary methods of analysis—enables them to respond to, entrain, penetrate and become retained in the tumor microenvironment because of aspects of its physical nature common to different solid tumors. Indeed, poly(*N*-isopropyl methacrylamide)s and related polymers are known to exhibit a wide variety of environmentally-responsive bulk properties, including changes in volume, solubility, and aggregation, as a function of changes in factors such as temperature, ionic strength, and concentration. Exploration of these phenomena from a physical chemistry and materials point of view is beyond the scope of this manuscript, but is the subject of ongoing studies in our laboratories.

Overall, nanostructures of the SANG type that are responsive to changes in their physical environment represent an important

https://doi.org/10.1038/s41467-025-66788-4

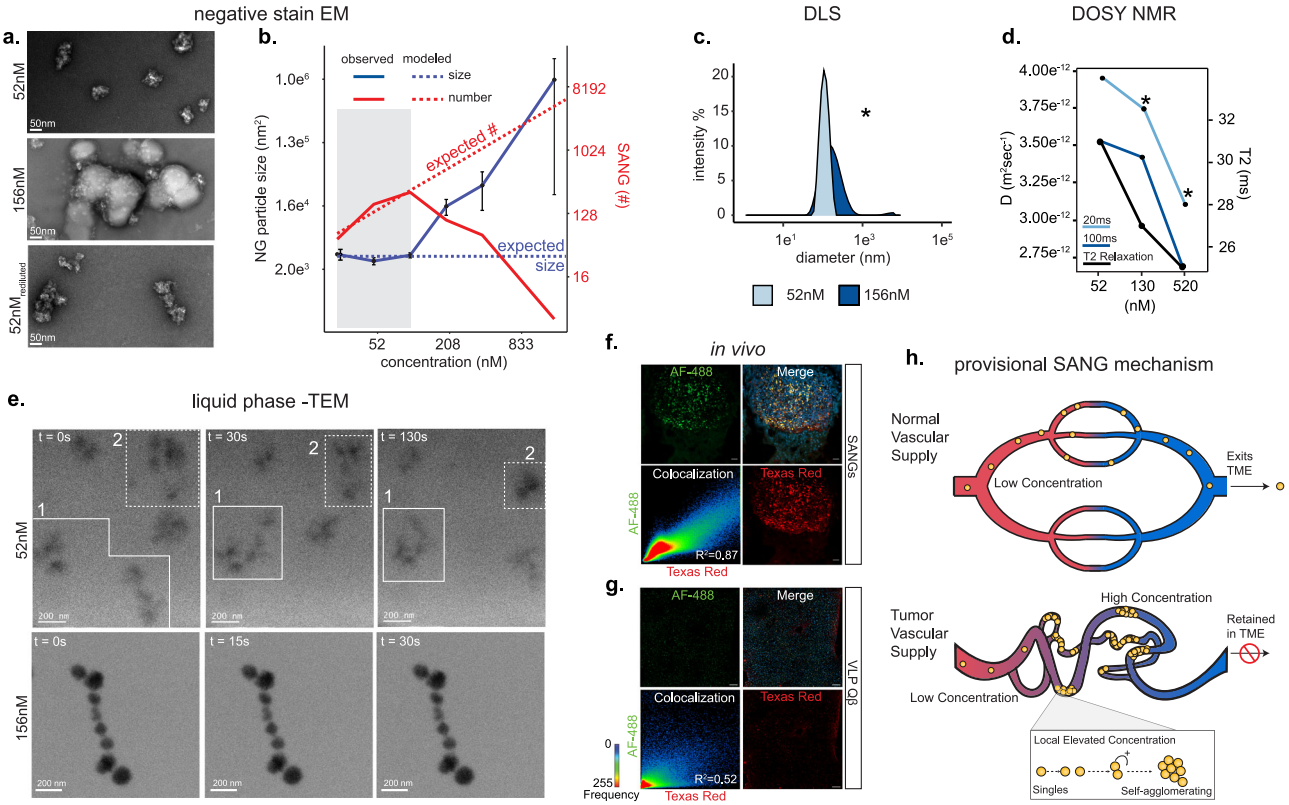

Fig. 6 | Tests of tumor-agnostic delivery mechanism. a Representative phase contrast transmission electron microscopy (TEM) image showing reversible SANG agglomeration when going from 52 nM to 156 nM, and back again (re-diluted), $n = 3$ independent experiments. **b** Observed (solid lines, data points = mean ± sd) and expected (dotted lines) size and number of SANGs particles over the entire concentration range studied by TEM within a standard area field of view ($n = 3$ replicates). **c** Hydrodynamic size distributions of SANGs at 52 nM and 156 nM concentrations ($n = 3$ independent experiments- Wyatt DLS). **d** Diffusion coefficients derived from diffusion-ordered NMR (DOSY) for 20 ms and 100 ms pulse sequences and T2 relaxation times across a 10-fold concentration range. **e** Sequence of representative liquid phase transmission electron microscopy (LP-TEM) images (full data in Supplementary Movie 4) showing two instances (outlined regions) of SANG agglomeration at 52 nM and the persistence of self-adhered particles at 156 nM ($n = 3$ replicates). **f** Representative high-resolution (63x) maximal projection confocal microscopic image of a colon tumor showing a merged view of both fluorescently labeled SANG populations and DAPI. Scatter plot of pixel-based colocalization analysis of representative areas (Costes randomization-based colocalization $R = 0.87 \pm 0.02$, $p < 0.001$, $n = 3$ animals, 3 sections each); a value of 0.5 indicates purely random co-localization probability. **g** Representative high-resolution (63x) maximal projection confocal microscopic image of a healthy liver showing a merged view of both fluorescently labeled Qβ VLP populations and DAPI. Scatter plot of pixel-based colocalization analysis of representative areas (Costes randomization based colocalization $R = 0.52 \pm 0.02$, $p < 0.001$, $n = 3$ animals, 3 sections each). **h** Graphical depiction of the provisional mechanism by which SANGs achieve preferential tumor by exploiting maladaptive vasculature observed uniquely in tumor microenvironments (bottom) compared to healthy vasculature (top). (*) indicates statistically significant differences between experimental groups as empirically derived from a hierarchical Bayesian model (stan_glm): 95% highest density intervals do not overlap between groupwise contrasts.

development in systemic delivery of RNAi to solid tumors, as they exhibit exceptionally selective distribution and low toxicity in vivo. The delivery of other molecular payloads may also be envisioned, if the advantageous functional dynamics of SANGs are retained in such cases.

Methods

Animal studies

Six- to eight-week-old female NOD.CB17-Prkdc^{scid} IL2rg^{tml}/BcgenHsd (B-NDG: Envigo), NOD.CB17-*Prkdc*^{scid}/NCrCrl (NOD SCID), C57BL/6, and CD-1 Mice (Charles River) were maintained at the Georgia Institute of Technology's Physiological Research Laboratory in individually ventilated and watered cages kept at negative pressure. Immunodeficient animals were housed under pathogen-free conditions according to Association for Assessment and Accreditation of Laboratory Animal Care guidelines. The mice were kept in rooms on a 12 h light/dark cycle with ambient temperature between 22.8 and 23.9 °C with 30–40% relative humidity. The experiments were only performed during the light phase. Sterile food (Alfalfa Free Imaging Lab Diet) and sterile water was provided to mice ad libitum. The mice were acclimatized for at least 6 days before the beginning of the experiments. The animals were randomly distributed among the experimental groups. Researchers were blinded to the animal group allocation during data acquisition. The animals were euthanized by isoflurane overdose (5%) and exsanguination.

Six-month male and eight-month-old F344/NTac-*Apc*^{am1137} (Pirc) and F344 rats (Rat Resource & Research Center), ten- to fourteen-week-old Sprague Dawley-*Rag2*^{em2hera}*Il2rg*^{em1hera}/*HblCrl* (SRG), Sprague Dawley (Charles River), Sprague Dawley HsdSage:SD-*Rag2*^{em1sage} (Rag2) (Envigo), and were maintained at the Georgia Institute of Technology in individually ventilated and watered cages kept at negative pressure. Immunodeficient animals were housed under pathogen-free conditions according to Association for Assessment and Accreditation of Laboratory Animal Care guidelines. The rats were kept in rooms on a 12 h light/dark cycle with ambient temperature between 22.8 and 23.9 °C with 30–40% relative humidity. The experiments were only performed during the light phase. Sterile food (Alfalfa Free Imaging Lab Diet) and sterile water were provided to rats ad libitum. The rats were acclimatized for at least 6 days before the beginning of the experiments. The animals were randomly distributed among the

https://doi.org/10.1038/s41467-025-66788-4

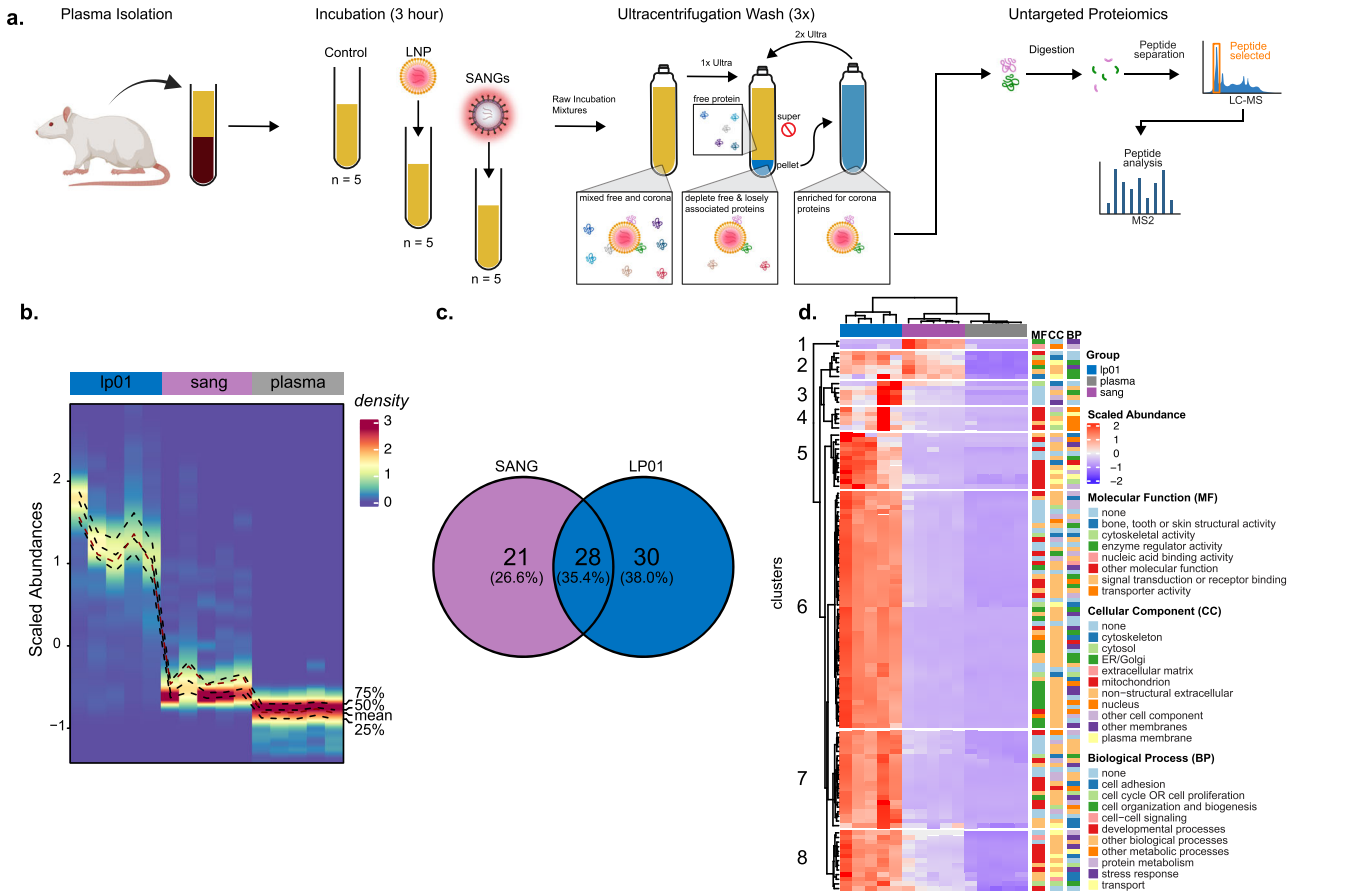

Fig. 7 | Comparative proteomics profiling of individual nanoparticle platform coronas. a Schematic illustration of the multi-platform comparative protein corona study created with BioRender. Plasma freshly isolated from healthy Wistar rats were aliquoted and incubated with either LNP or SANG nanoparticles for 3 h ($n = 5$ replicates per group). A control plasma sample was included to measure background plasma contamination retained through the wash steps. After incubation, ultracentrifugation washing (3x) removed free and non-specifically bound biomolecules. After each wash, the pellet was resuspended in buffer. After the final wash, proteins were digested in preparation for untargeted proteomics analysis by LC–MS. **b** Density heatmap shows scaled total protein abundances detected on protein corona of each nanoparticle platform ($n = 5$, biologic replicates) after ultracentrifugation washing. Plasma samples ($n = 5$, biologic replicates) were included to show residual uncomplexed plasma proteins not removed by identical ultracentrifugation (3x) washing of nanoparticle platforms and provide background protein level control for comparison. Mean (solid), 25%, 50%, and 75% (dotted) lines indicate quantiles. **c** Venn diagram shows the number (%) of shared and unique corona proteins associated with different nanoparticle platforms after filtering for FDR < 0.001 and > 1.5-fold-change compared to plasma proteins. Unique and shared proteins are described in Supplementary Data 1. **d** Hierarchical clustering of nanoparticle platforms. Vertical clustering displays similarities between samples, while horizontal clusters reveal the relative abundances and groups of proteins that distinguish nanoparticle platforms. Red and blue indicate higher and lower than the mean protein signal, respectively. Scale bars represent row Z-scores. Color-coded top molecular function (MF), cellular component (CC), and biologic process (BP) associated with each protein. Proteins and abundances in each numbered cluster (1–8) are detailed in Supplementary Data 2.

experimental groups. Researchers were blinded to the animal group allocation during data acquisition. The animals were euthanized by isofluorane overdose (5%) and exsanguination.

Ten- to fourteen-week-old Sprague Dawley rats with chronically catheterized left jugular veins (Charles River) were used for pharmacokinetic and toxicity studies and handled as described above, with the following exceptions. Rats were singly housed to avoid disruption of the Vascular Access Buttons™ (Instech), and catheter patency was maintained by flushing (heparinized saline 500 units/mL) and locking (heparinized dextrose: 500 units/mL in dextrose 50%) catheters every 5–7 days.

All animals were cared for according to the Georgia Institute of Technology Physiological Research Laboratory policies and under ethical guidance from the university's Institutional Animal Care and Use Committee (IACUC: A100128) or Global Center for Medical Innovation (GCMI) T3 Labs with Institutional IACUC: GT94Rr/A100632) following National Institutes of Health guidelines.

A sexually mature (6-month) female Domestic Yorkshire Crossbred Swine weighing 73 kg was studied at Global Center for Medical Innovation (GCMI) T3 Labs with Institutional IACUC approval. The Test Facility is accredited by the Association for the Assessment and Accreditation of Laboratory Animal Care, International (AAALAC) and registered with the United States Department of Agriculture to conduct research in laboratory animals (T311P/A1004210). Before treatment, a physical exam and clinical assessment were performed. After the swine was deeply anesthetized, an acutely placed jugular catheter was placed with ultrasound guidance for slow infusion of SANGs and serial blood sampling. At the conclusion of the study, the swine was euthanized via intravenous administration of KCL 1–2 meq/kg under a deep plane of anesthesia.

Tumor cell lines and cancer model induction

HEY-A8 gifted by Dr. Gordon B. Mills, (MD Anderson Cancer Center, Houston, TX) were stably transfected with pGL4.51 Luciferase Reporter Vector (Promega). The resulting HEY-A8-F8 cell lines and MDA-MB-231-luc2 (SC059-Puro) TNBC cell lines (GeneTarget) were maintained in RPMI 1640 (Mediatech) supplemented with 10% FBS (Fetal Bovine Serum; Atlanta Biologicals) and 1% antibiotic-antimycotic solution

(Mediatech). Media were supplemented with Geneticin G418 sulfate (GIBCO) and Puromycin (GIBCO) selective agents to maintain Luciferase expression. Adherent monolayer cultures were maintained at 37 °C in 5% CO_2.

For the establishment of the mouse TBNC model, 1 × 104 cells/50 μL saline were subcutaneously injected into the fourth mammary fat pads using a 27 gauge × 1/2 inch needle. For the establishment of the mouse primary OC model, 4 × 105 cells/100 μL saline were injected into the right ovary. For the establishment of the mouse metastatic OC model, 4 × 105 cells/100 μL saline were injected into the right lower quadrant of the abdominal cavity using a 27 gauge × 1/2 inch needle. For the establishment of rat metastatic lung cancer (MDA-MB-231) and OC models, between 1–2 × 106 cells/100 μL were injected in the right lower quadrant of the abdominal cavity using a 27 gauge × 1/2 inch needle.

SANG synthesis

SANGs were synthesized via emulsion precipitation polymerization. In a typical core nanogel synthesis, N-iso-propylmethacrylamide (NIPMAm) monomer (117.8 mM), N, N′-methylene-bis (methacrylamide) (BIS) cross-linker (6.2 mM) and sodium dodecyl sulfate (SDS) surfactant (8 mM) were dissolved in deionized H_2O. The solution was stirred under nitrogen, brought to 70 °C, and treated with 0.5 mL of a 10 mg/mL aqueous ammonium persulfate (APS) solution to initiate polymerization (800 mM). The reaction was carried out at 70 °C for 4 h with vigorous stirring under nitrogen. The resulting core particle reaction solution was passed through a 0.2 μm filter. Core particle synthesis was verified by DLS as having an unimodal distribution between 47–57 nm. The core nanogels were used as a seed for the addition of a shell layer. A mixture of NIPMAm (48.75 mM), BIS (1.0 mM), and aminopropyl methacrylamide (APMA, Polysciences, 0.25 mM) prepared in deionized H_2O (dH_2O) was added to the core seed. When the temperature stabilized at 70 °C, the reaction was initiated by adding a 0.5 mL aliquot of 0.05 M APS, and was allowed to proceed for 4 h under N_2 atmosphere. After cooling to room temperature, the reaction mixture was filtered through a 0.2 μm filter and the size of the crude core-shell nanogels was measured by multi-angle dynamic light scattering. SANGs were then purified and concentrated using a VivaFlow 50 R 100 kDa MWCO tangential-flow filtration (TFF) cartridge (Sartorius, circulation flow rate 10 mL/min, transmembrane pressure ≈2 bar), retaining the SANGS within the retentate while allowing small-molecule reagents to be removed. During the initial cleaning phase, the circulating volume was maintained by continual addition of dH_2O, corresponding to 10x volume of washing (for example, a 50 mL reaction volume was washed with 500 mL of dH_2O). After cleaning, no additional dH_2O was added, and the solution was allowed to concentrate by ~10-fold. Purified SANGs were re-checked with DLS, and then concentrated SANG solutions were flash frozen and lyophilized under vacuum. When reconstituted in aqueous media, SANGS swell back to their original size.

SANGs labeling

SANGs that were used for in vitro delivery and in vivo biodistribution studies were labeled with AF-488-NHS, Texas Red-NHS, or LiCOR IRDye® 800RS NHS ester following the manufacturer's protocol for labeling high molecular weight molecules, depending on the study needs. For example, SANGs were reconstituted in pH 8.4 PBS (1X) at 52 nM and were incubated with 1 mM LiCOR IRDye® 800RS NHS ester overnight at room temperature. Unreacted dyes were then removed by Pierce® Zeba™ Desalting Spin Columns following the manufacture's protocol.

siRNA species and labeling

Pre-miR™ miRNA Precursor for miR-429 (Cat #: AM17101, ID: PM10221) was purchased from Ambion™. Silencer® Select siRNA KRAS (Cat #: 4390822 s7940, Sequence: GCCUUGACGAUACAGCUAAtt), Silencer® Select siRNA EGFR (Cat #: 4390826 s564, Sequence: CCAUAAAUGCUACGAAUAUtt), Silencer® Select Negative Control #1 siRNA (Cat #: 4390843), and Silencer® Cy™3 Labeled Negative Control siRNA #1 (Cat #: AM4621) were purchased from Invitrogen.

siRNA species were fluorescently labeled per manufacturer's instructions using the Ulysis Alexa Fluor 647 Nucleic Acid Labeling Kit. Pre-conjugated Cy3-siRNA was purchased from Invitrogen.

Dynamic light scattering and multiangle laser light scattering measurements

SANGs were prepared as described for in vivo usage with a final concentration of 1.0 mg mL^{-1} in PBS (1X pH 7.4). For size analysis, a 10 μL aliquot was diluted into 990 μL dH_2O or saline at pH 7.4 and analyzed using a Malvern Zetasizer Nano ZS instrument and validated with a DynaPro® NanoStar® instrument. For zeta potential measurements, a 0.4 mL aliquot of the standard particle solution was diluted in 4.6 mL dH_2O at pH 7.4 and loaded into a Malvern capillary for analysis. Concentration-dependent changes in hydrodynamic size were measured by increasing the initial dry weight of SANGs used to generate starting solutions. Dilution challenged studies by dynamic light scattering (DynaPro® NanoStar®) were accomplished by diluting solutions from a starting concentration of 0.1 mg/mL in PBS (1X pH 7.4).

Multiangle laser light scattering (MALLS) (Wyatt Technology Corporation, Santa Barbara, CA) was used to determine the molecular weight for all SANGs at 25 °C. Major physiochemical measurements were independently validated by the National Cancer Institute's National Characterization Laboratory (NCL). Raw data and reports are included in Supplemental Information.

Electron microscopy measurements

For conventional TEM, 3 μL of the sample solutions were prepared for negative stain using formvar/carbon 200 mesh copper grids. The grids were previously glow-discharged (negative charge) for 15 s using a GloQube Plus glow discharge system (Quorum Tech). Samples were then stained with 2% uranyl acetate for one minute. The images were collected using a JEOL JEM-1400 transmission electron microscope operating at 80 keV equipped with a Gatan US1000 2kx2k CCD camera.

The micrographs were collected at a nominal magnification of ×20,000, on a 2048 × 2048 pixels charge-coupled device camera (UltraScan 1000, Gatan), yielding a pixel size of 5.1 Å. The overview images were collected at ×2000 (52 Å per pixel). Dilution challenged studies were accomplished by ten-fold dilution in dH_2O of samples previously analyzed by TEM.

Liquid phase TEM

Commercially available silicon nitride microchips (Protochips Inc.) were used for imaging of soft nanohydrogels with TEM. At all concentrations, liquid cell top chips (EPT-52W-10) were used. At low concentration, 0.0263 μM, bottom chips (EPB-52BNS-10) with a static spacer size of 50 nm were used, while at medium and high concentrations, 0.105 μM and 0.210 μM respectively, bottom chips (EPB-52DNS-10) with a static spacer size of 150 nm were used to account for the increase in structure size that is dependent on concentration. All chips underwent a 2-min immersion in acetone to remove the photoresistant coating and were subsequently immersed in ethanol for another 2 min. Excess ethanol was blotted off with filter paper, and the chips were further dried by flowing N_2 gas across the surface. Following the cleaning, the chips were surface treated by glow discharge in a PELCO easiGlow system at 0.39 mBar, 15 mA for 45 s and held for 10 s to render the surfaces hydrophilic and to increase wettability. The chips were then assembled into a Poseidon Select holder with 0.6 μL of sample.

Experiments began with either 0.5 or 1 mg of lyophilized soft nanohydrogels. Samples were then diluted to the desired

concentration with Millipore DI water. To avoid larger particles obstructing the hermetic seal of the top and bottom microchips, the diluted samples were filtered using a 0.2 μm syringe filter and then added to the liquid cell.

In-situ experiments were conducted on a FEI Tecnai F30 TEM with a thermal field emission gun operating at 200 kV in the Materials Characterization Facility of the Institute for Matter and Systems at Georgia Institute of Technology. Videos of the soft hydrogels were collected using a Gatan Oneview Camera and recorded using the Digital Micrograph software. The electron beam dose rate was calibrated to 30 $e^-/Å^2s$ at a camera magnification of 19.5kx with an in-house Digital Micrograph script. All videos were collected at 4096-by-4096 pixels and a frame rate of 15 frames per second. Corresponding images were binned by summing with Digital Micrograph to a frame rate of 1 frame per second to increase contrast between soft nanohydrogels and the background.

Particle analysis

The following procedure with ImageJ was used for the analysis of all images, repeated 5 times ($N = 5$) for each condition. (1) Each raw TEM image (grayscale) was converted to binary (sequentially using Image, Adjust, and Threshold parameters); an upper boundary of 109–178 was set depending on contrast and Dark background option, and a lower cutoff of ≈0 was used. (2) The resulting binary image was segmented using ImageJ's standard watershed process (sequential Process, Binary, and Watershed functions). (3) Segmented particle sizes were determined with the particle analysis functions Analyze and Analyze Particles (size range = 100 to infinite (pixel)^2 units, circularity = 0–1, showing bare particle outlines). (4) Particle diameters were determined from the ImageJ area output using spherical approximation.

SANGs preparation and RNAi loading for in vitro and in vivo studies

Before delivery to cell cultures or to animals, SANGs were either reconstituted in sterile saline (0.5%) for delivery studies (Fig. 1g, h) and biodistribution (Fig. 4) or were loaded with RNAi payloads for efficacy and delivery studies (Figs. 2–5)[30]. Briefly, lyophilized SANGs were reconstituted in RNAi solutions (20 μM in sterile saline 0.5%) to a final concentration of 16–17 μg siRNA mg^{-1} of SANGs. SANGs were incubated at room temperature for 60 min before being loaded into syringes for i.v. delivery. Under these conditions, the swelling of the SANGs particles almost completely incorporates all of the solution volume, thereby loading the payload in the particles with high efficiency. At 16.5 μg siRNA (1.2 nmol of 21-mer duplex -) siRNA per mg of SANGs (composed of approximately 30 weight-percent shell, containing approximately 11.7 nmol of aminopropyl-containing monomer), the N:P ratio is approximately 0.24.

SANGs stability in RNase

To test stability in pure RNase conditions, SANGs were loaded with siRNA against *EGFR* as described above. RNase was then added to the solution to a final concentration of 0.03 mM and incubated at RT for one hour. This final solution was then added to the complete cell culture media for HEY cells. We include three additional conditions as control: 1) untreated cells, 2) cells treated with standard siRNA-loaded SANGs, and 3) SANGs loaded with siRNA that was pre-treated with 0.03 mM RNase. Forty-eight hours after transfections, cells were collected and *EGFR* RNA expression was quantified by RT-PCR as described below.

SANGs and SANG-siRNA stability in serum

To test stability in high serum conditions (in vivo simulation), Hey-A8-F8 cells were initially plated in well plates (Ibidi Cat.No: 80807) at 2 × 104 cells/well and then incubated at 37 °C and 5% CO_2 in RPMI 1640 (Mediatech) supplemented with 10% FBS (Fetal Bovine Serum; Atlanta Biologicals) and 1% antibiotic-antimycotic solution (Mediatech). Twenty-four hours after plating, the media was exchanged for solutions containing 50% or 90% FBS. Unloaded SANGs (AlexaFluor-647 labeled) and SANGs (AlexaFluor-647 labeled) loaded with Cy3-labeled siRNA were then added to wells and allowed to incubate for 18 h. Immediately prior to imaging, incubation solutions were removed and cells were washed 3x with PBS (1X pH 7.4), and nuclei were counterstained with Hoechst. Live cell imaging in a temperature and CO_2 chambered confocal microscopy (Olympus FV4000) was acquired with a 20x objective (N.A. = 0.8) at a step size of 1 μm. Laser strength, gain, and other critical image acquisition parameters were held constant when imaging across treatment groups.

Entrainment of RNAi in SANGs

Encapsulation efficiency was determined via ultracentrifugation of the SANG loading solution and measurement of supernatant siRNA concentration by UV-vis spectroscopy (Shimadzu UV-1601). siRNA concentration in the loading solution and supernatant (after SANG swelling was complete) were determined via interpolation from a separately constructed standard curve of absorbance *vs.* concentration. Encapsulation efficiency (EE) was calculated by equation 1[30].

$$EE = \frac{m_{\text{siRNA loading}} - m_{\text{siRNA supernatant}}}{m_{\text{siRNA loading}}} \times 100 \quad (1)$$

SANG delivery, internalization, and endosomal escape measurements

Labeled SANGs with or without RNAi payloads were reconstituted in culture media and transferred to well plates (Ibidi Cat. No: 80807) containing 2 × 104 cells/well and then incubated at 37 °C and 5% CO_2. After the appropriate incubation period, cells were either subjected to live cell imaging in a temperature and CO_2 chambered microscope or fixed with 4% paraformaldehyde for 15 min at room temperature, washed 3x (5 mins per wash) in PBS (1X pH 7.4), then permeabilized treated with 0.3% Triton X in PBS (1X pH 7.4), and stained following immunofluorescence protocol described below.

For cell uptake mechanism studies, cells were exposed to several different concentrations of the inhibitors: NaN_3 (0, 25, 50 μM), Cpz hydrochloride (0, 50, 100, 200 μM), Mβcd (0, 0.5, 1, 2 mM), CytD (0, 50,100, 200 μM), and LatA (0, 2, 4 μM). For endosomal escape studies, both fluorescently labeled wheat germ agglutinin and CellLight™ Lysosomes-RFP, BacMam 2.0 were used to track endosome and lysosomal populations. The degree of colocalization was quantified based on Pearson's correlation coefficient (R) using the ZEN blue (Zeiss) colocalization module. Here, regions of interest (ROIs) were drawn around each individual cell based on membrane staining (actin or lectin derivatives). Costes algorithm[63] then determined the thresholds of two fluorescent channels at a time, the software automatically calculated pixel intensity spatial overlap coefficients between them using colocalization coefficients described by the number of pixels colocalized in one fluorescent channel divided by the total number of pixels, meaning values approach 0 as fluorophores are less colocalized.

Cell isolation from organs, staining, and flow cytometry

Cells were isolated 3 h after i.v. administration of LNP-LP01 formulated to carry AlexaFluor-647 labeled siRNA against *EGFR* ($n = 3$ biologically independent experiments), SANGs formulated to carry AlexaFluor-647 labeled siRNA against *EGFR* ($n = 4$ biologically independent experiments), or PBS (1X pH 7.4) control. Animals were immediately transcardially perfused with 5 mL of PBS (1X pH 7.4). Organs were isolated immediately following perfusion. Livers and kidneys were cut and then placed in a digestive enzyme solution with collagenase type I (Sigma-Aldrich), collagenase type XI (Sigma-Aldrich), and hyaluronidase (Sigma-Aldrich) at 37 °C and 500 rpm for 30 min. Digested tissues were

passed through a 70 μm filter. Cells were stained to identify specific cell populations using flow cytometry. Antibody clones used for staining were anti-CD31 (390, BioLegend), antiCD45.2 (104, BioLegend). Cell populations were first gated for non-debris (forward scatter versus side scatter), then gated for singlets (forward scatter versus forward scatter width) and viable cells (Zombie). The viable, single cells were analyzed for AlexaFluor-647 positivity to determine the percentage of AlexaFluor-647-positive cells in each sample. The AlexaFluor-647 median fluorescence intensity was normalized to the autofluorescence of each tissue type, as determined using samples from PBS (1X pH 7.4) injected mice. Representative gating strategies for liver and kidney cell populations are included in Supplementary Fig. 16.

Lipid nanoparticle (LNP-LP01) formulation and characterization

LNP-LP01 (designated LNP-INT01 in this reference[38]) were formulated in a Precision Nanosystems Ignite system by mixing siRNA against *EGFR* (Invitrogen 4390824) conjugated with Alexa Fluor 647 in citrate buffer with the stereopure ionizable lipid LP01, DMG-PEG2K (Avanti Lipids: #880151), cholesterol (Avanti Lipids #700100), and DSPC (Avanti Lipids #860365) in 100% ethanol. They were mixed at a total flow rate of 12 mL/min. LNP hydrodynamic diameter was measured using dynamic light scattering (DLS, DynaPro Plate Reader III, Wyatt Technology). LNPs were diluted in sterile PBS (1X pH 7.4) to a concentration of ~0.08 μg/mL and analyzed. Their diameter was ~40 nm and monodisperse. They were then dialyzed in PBS (1X pH 7.4) and sterile filtered with a 0.22 μm filter.

Laser scanning confocal microscopy

Tissue sections were imaged using laser scanning confocal microscopy (LSCM) (Zeiss Biosystems, 900). Tile scans of large tissue or well areas were acquired with a 20x objective (N.A. = 0.8). Z stacks of tissue sections or high-resolution cell imaging (well plates) were acquired with a 63x objective (N.A. = 1.4) at a step size of 0.5 μm. Laser strength, gain, and other critical image acquisition parameters were help constant when imaging across treatment groups. For each 8-well plate experiment, we include a negative and a positive control group on which the imaging parameters are first set. Stacks of images were processed and analyzed using Imaris (Bitplane) or ImageJ (NIH) imaging software. Figures present images as either flat maximal projections of the sum of the z-axis optical slices or three-dimensional renderings of z-stacking of two-dimensional scanning images from different depths. Analyses were performed by an investigator blinded to treatment group and was determined by measuring the mean fluorescence intensity observed on the flat maximal projections of the z-stack images, respectively.

Cell toxicity assay

The toxicity of various unloaded and loaded SANGs were determined by Tox 8 Assay. Cells incubated for overnight with unloaded and loaded SANGs (Fig. 1) were then washed with PBS (1X pH 7.4), the medium was replaced, and the cells were incubated for an additional 72 h in medium. The Tox 8 reagent (Sigma) was added to the cells according to the manufacturer's instructions. The fluorescence at 590 nm was read after 1 h, and the extent of cellular viability/proliferation was determined.

Tissue harvesting

Following in vivo studies, animals received a lethal dose of isoflurane anesthesia (5%) until respiration rates dropped below 10 beats/min. Then, the animals were transcardially perfused with vascular rinse containing heparin, followed by ice-cold 4% paraformaldehyde (PFA) in 0.1 M phosphate buffer (PB, pH = 7.4). Tissues were extracted and post-fixed overnight in 4% PFA at 4 °C. The following day, all tissue was transferred and stored in a 30% sucrose cryoprotectant solution until sectioning took place. For immediate ex vivo analysis following in vivo biodistribution studies, animals were exsanguinated without transcardial perfusion. Following immediate ex vivo imaging, organs were either (1) drop fixed in 10% NFB or 4% PFA for ~24 h prior to downstream histological analysis or (2) were washed with sterile saline and immediately flash frozen (fresh) in 2-methylbutane (isopentane) pre-chilled in liquid nitrogen, then stored at −80 °C for PCR analysis.

Histological methods and immunofluorescence

Tissue sections were sectioned at a thickness of 50 to 75 μm on a cryostat (Leica model# CM 3050 S) and collected directly onto charged (+) microscope slides for further histological processing. Sections from all treatment groups were processed simultaneously[42]. Sections were washed 3x (10 mins per wash) in PBS (1X pH 7.4) with 0.3% Triton X-100 (PBST) and then blocked for 1 h in 10% normal donkey serum diluted in PBST. Sections were then incubated overnight at room temperature in primary antibodies diluted in blocking buffer (5% normal goat serum, PBST). The primary antibodies used were as follows: mouse monoclonal anti-EGRF (SC-120, Santa Cruz Biotechnolgy, 1:100), mouse polyclonal anti-EGFR antibody (PA1-1110, Invitrogen, 1:100), and mouse monoclonal anti-KI67 (SC-23900, Santa Cruz Biotechnology, 1:100). The following day, tissue sections were washed again 3x in PBST and immunoreactive sites were revealed with species-specific fluorescent-conjugated secondary antibodies (Jackson ImmunoResearch Laboratories). Following a 2 h incubation in the secondary mixture at room temperature, sections were washed 3x in PBS (1X pH 7.4), mounted, and coverslipped with Vectashield (Vector Labs, Newark, CA, H1000).

PCR

RNAs were isolated using the mRNeasy Micro KIT (Qiagen, Germantown, MD). After total RNA quantification by NanoDrop, RNA concentration and integrity were assessed on the Bioanalyzer RNA Pico Chip (Agilent Technologies, Santa Clara, CA), and complementary DNA was prepared using the high-capacity complementary DNA reverse transcription kit (Applied Biosystems, Thermo Fisher Scientific). Quantitative PCR experiments were performed using the Fast Advanced Master Mix (Thermo Fisher Scientific). GAPDH was used as a reference control gene for analysis of differential expression.

Whole-body luminescence and fluorescent imaging and ex vivo imaging

Tumors were induced in groups of five mice as described above (**Tumor cell lines and cancer model induction**). Tumor growth was monitored by bioluminescent imaging following intraperitoneal injection of d-luciferin (15 mg/kg). Bioluminescence analysis was conducted using the Living Image software (PerkinElmer Inc.). Once tumors grew to the appropriate size, animals were randomly assigned to different experimental groups depending on the experimental design. Animals then received intravenously administered unloaded or loaded SANGs (1 mg kg^{-1} unless otherwise noted). Controls include free FAM-siRNA, free-fluorescence dye (Texas Red-NHS ester or LiCOR IRDye® 800RS NHS ester) and unlabeled SANGs at the same SANG equivalent doses. At 4, 24, 48, 72, and 288 h time points, the animals were imaged on black paper with IVIS SpectrumCT (PerkinElmer). After whole-body imaging, animals were euthanized. Tumors and various organs were excised for ex vivo imaging. Tumor-free wild-type mice (C57BL/6 and CD-1) injected with SANGs or free FAM-siRNA were used as controls.

Quantification of ex vivo biodistribution was performed as follows. Background tissue auto-fluorescence was subtracted by normalizing all tissues to that measured in each animal's cardiac tissue, which was empirically determined to be the lowest absolute value across all measured organs. We then computed the fold-changes for each organ system. In this way, all cardiac tissues had fold-change values of 1.0, and every other tissue had values greater than 1.0. This allows reliable and realistic subtraction of auto-fluorescence effects across species and strains.

Metastatic targeting analysis

To quantify the specificity of metastatic targeting by SANGs, tumor BLI and SANG fluorescent images (acquired with IVIS SpectrumCT (PerkinElmer)) were imported into ImageJ software and subjected to colocalization analysis with JACoP plugin (v2.1.4). A total of 5 independent animals were utilized for analysis.

Pharmacokinetics and excretion studies

To define the pharmacokinetics of SANGs, blood was collected in EDTA-containing tubes at pre-treatment, 5 min, 0.5 h, 1 h, 2 h, 4 h, 24 h, and 48 h time points from chronically implanted left-jugular catheters. Blood (100 μL) was plated from each time point for each animal on a 96-well plate and imaged by IVIS SpectrumCT (PerkinElmer). Fluorescence signal was normalized within each animal based on its pre-treatment value and its maximal initial dose value, then averaged across all animals ($n = 5$).

For the excretion studies, animals were singly housed in metabolic cages and provided with food and water ad libitum. Loaded SANGs and unloaded FAM-siRNA formulations were administration i.v. via a chronically implanted left-jugular catheter at 1 mg•kg^{-1}. Urine and feces were collected from over 0–1, 1–3, 3–9, and 9–24 h time periods post-administration. Fluorescent signals from urine and feces were imaged by IVIS SpectrumCT (PerkinElmer) and analyzed by Living Image Software (PerkinElmer).

Toxicity & tolerability studies

Two 7 mg•kg^{-1} doses i.v. of either (1) empty SANGs or (2) SANGs loaded with scrambled miRNA and siRNA to female CD-1 mice (5 animals/group). Daily weight changes were recorded, and terminal serum blood chemistry was analyzed 14 days after the final dose.

Two clinical applications of SANGs were simulated. First, SANGS (7 mg•kg^{-1}) loaded with siRNA against EGFR were i.v. administered to female NOD-SCID mice with fully developed OC tumors. Twenty-four (24) h after the SANG dose, cisplatin (10 mg•kg^{-1}) was i.p. administered. Potential test article-related effects were evaluated by the assessment of clinical signs and body weight. In separate cohorts of identically treated experimental animals, serum blood chemistry and inflammatory markers were evaluated 24 h after cisplatin treatment.

Pirc rats ($n = 5$ male), at least 6-month-old at initiation of dosing, were treated with SANGs loaded with siRNA against *EGFR* followed by an i.p. dose of oxaliplatin (5 mg•kg^{-1}) 24 h later. This was repeated twice weekly for four weeks. Potential repeat dose test article-related effects were evaluated by the assessment of clinical signs and body weight.

A maximum tolerated dose (MTD) study was conducted in female and male Sprague-Dawley rats (obtained from Charles River Laboratories), 8–10 weeks old at initiation of dosing. SANGs loaded with siRNA against *EGFR* was administered at 0, 7, 12, 17 mg•kg^{-1} (3 animals/sex/group) via single intravenous injection in catharized jugular vein. Approximately 0.3 mL of blood was obtained 6- and 24-h post-dose from jugular catheters of conscious animals using manual restraint and was processed to serum. All groups were terminated 24 h post-dose for postmortem evaluation. Potential test article-related effects were evaluated by the assessment of clinical signs, body weight, serum chemistry (ANTECH-GLP), macroscopic observations at necropsy, and histopathology Emory University School of Medicine Department of Pathology and Laboratory Medicine).

NMR measurements

NMR spectra (Bruker DRX-500 or Bruker AV3 HD-700) in D_2O were recorded with chemical shifts (δ) set relative to residual water at 4.65 ppm. DOSY NMR provided diffusion coefficients using the 2D ^{1}H DOSY double stimulated-echo (dstegp3s) pulse sequence (longitudinal eddy current delay = 20 ms, gradient recovery delay = 100 ms) to compensate for convection effects. Data were processed using TopSpin (Bruker), and diffusion coefficients were obtained by fitting the integrations of several ^{1}H signals to the Stejskal–Tanner expression.

In vivo agglomeration measurements

SANGs were conjugated to either AF-488-NHS or Texas-Red-NHS, resulting in two fluorescently distinct populations. These two populations were then i.v. administered via the lateral tail vein to Pirc rats ($n = 5$). The animals were euthanized 48 h after administration, and major organs and colorectal tumors were extracted as described (**Tissue Harvesting**) and processed for LSCM. Tissues were treated only with DAPI and Lectin-DyLight™ 649 (Vector Laboratory: DL-1178-1) to label nuclei and cell bodies, respectively. Tissues were then imaged as described in **Laser scanning confocal microscopy**. The degree of colocalization was quantified based upon Pearson's correlation coefficient (R) using the ZEN blue (Zeiss) colocalization module as described. We analyzed 20x organ-wide images (Fig. 7e, Figure S ZZZ) and expanded 63x images (Figure 7e1–2) to (1) quantify specific regions of interest (pixel-based), (2) perform object-based colocalization analysis, and (3) quantify the size of SANG agglomerates that colocalize compared to isolated SANGs (Fig. 7f).

Expression and purification of Qβ VLPs

Qβ virus-like particles were prepared and isolated as previously described[64]. Briefly, competent BL21(DE3) cells were transformed with a pCDF vector coding for the Qβ coat protein and grown for 24 h on SOB-agar containing streptomycin (50 μg/mL). A single well-isolated colony was cultured overnight in 50 mL of SOB media (containing streptomycin at the same concentration) and then diluted into 500 mL of selective SOB media and incubated at 37 °C. Protein expression was induced by isopropyl β-d-1-thiogalactopyranoside (IPTG, 1 mM final concentration) added to cultures of OD 0.7–0.9, followed by incubation for 5 h at 37 °C. The resulting cells were collected by centrifugation (JA-16.25 rotor, 10,000 rpm = 24,000 x g, 10 min, 4 °C) and frozen at −80 °C.

Frozen cell pellets were thawed and dispersed in 0.1 M K-phosphate buffer (pH 7.4) and then disrupted by probe sonication on ice (75 W, cycles of 5 s on and off, total sonication time 10 min). The lysed material was cleared by centrifugation (JA-17 rotor, 14,000 rpm = 27,000 × g, 10 min, 4 °C). VLPs in the clarified supernatant were precipitated by the addition of ammonium sulfate to a final concentration of 27% (w/v) with gentle shaking at 4 °C overnight. The resulting protein pellet was obtained by centrifugation under the same conditions (JA-17 rotor, 14,000 rpm = 27,000 × g, 10 min, 4 °C) and then resuspended in fresh 0.1 M potassium phosphate buffer.

To remove lipids and insoluble debris, a biphasic extraction was performed by adding a 1:1 (v/v) mixture of n-butanol and chloroform. After centrifugation (JA-17 rotor, 14,000 rpm = 27,000 × g, 10 min, 4 °C), the aqueous phase containing VLPs was recovered and further purified by sucrose gradient ultracentrifugation (10–40% w/v sucrose, SW28 rotor, 28,000 rpm = 140,000 × g, 4 h). Bands defined by visible particle layers were collected, and the VLPs were concentrated by pelleting at 440,000 x g (Beckman 70Ti rotor, 68,000 rpm, 2 h). The final pellets were isolated and resuspended in 0.1 M potassium phosphate buffer, and sterile filtered (0.2 μm PTFE syringe filter).

Fluorescent labeling of Qβ VLPs

Qβ VLPs were fluorescently labeled using AlexaFluor 647 (AF647) N-hydroxysuccinimide (NHS) ester, AlexaFluor 594 (AF594) NHS ester, or fluorescein NHS ester. Individual 1 mL solutions of Qβ VLPs in potassium phosphate buffer (pH = 7.8, 2 mg/mL in VLP, approx. 0.85 μmol in amine groups) were treated with the respective NHS ester reagent: AF594 (34 μL of 25 mM stock solution, 0.85 μmol), AF647 (70 uL of 12 mM stock solution, 0.85 μmol), fluorescein (50 uL of 42 mM stock solution, 2 μmol). The reactions were allowed to proceed

for 3 h at room temperature, protected from light on a rotor for gentle mixing. Each reaction was purified by two subsequent 7 K molecular weight cutoff Zeba™ Desalting Spin Columns following the manufacture's protocol.

Characterization of Qβ VLPs

The Qβ VLPs were characterized by dynamic light scattering (DLS, Wyatt DynaPro) to verify their size and check for aggregation. The overall protein concentration was determined by Bradford assay, using Pierce® Coomassie Plus Protein Reagent according to the manufacturer's protocol. The average number of fluorescent dyes attached to each particle (36 AlexaFluor 647, 36 AlexaFluor 594, and 9 fluorescein) was determined by mass spectrometry of denatured VLP samples prepared by passage through C4 ZipTip®, using both LC-MS ToF and MALDI methods (Supplementary Fig. 24). Assuming equal detection sensitivities, the ratio of peak intensities of coat proteins (CP) with *vs.* without an attached dye molecule is multiplied by 180 CP per particle to obtain the particle dye loading (for example, a ratio of 0.2 translates to approximately 36 dyes per particle); no coat proteins with more than one attached dye were detected.

Co-localization of fluorescent VLPs in liver

C57BL/6 mice were treated i.v. with 100 μL of a solution containing an equal mixture (25 μg each) of Qβ(AF594) and Qβ(fluorescein) ($n = 3$ mice). The mice were euthanized 1 h after i.v. injection, and the livers were extracted and post-fixed as described in **Tissue Harvesting**. Livers were sectioned and imaged by confocal microscopy as described in **Histological methods and immunofluorescence** and **Laser scanning confocal microscopy**, and co-localization analysis of the two fluorophores was performed.

Comparative proteomic analysis

Serum protein adsorption was conducted according to a modified method described previously[65]. Thus, 100 μg of LP-01, PLGA, and SANG were resuspended in 250 μL of complete rat serum and incubated at RT for 3 h. A fourth sample of serum without particles was used as a control and was subject to the same conditions as the particles. The samples were then washed with two cycles of ultracentrifugation (160,000 g, 2 h) and resuspension in 250 μL DPBS to remove unbound proteins. The final samples were resuspended in 50 μL DPBS for analysis.

An aliquot of 1 μg/ 1 μL in 50 μL solutions of proteins was used for proteolytic digestion. Micro s-Trap (Protifi) columns were used for tryptic digestion as per the manufacturer's instructions. In brief, 50 μg dried protein were resuspended in 23 μL SDS lysis buffer. Proteins were reduced by adding TCEP (final concentration 5 mM) and incubated at 55 °C for 15 min. The resulting samples were alkylated with iodoacetamide (10 mM) at room temperature for 15 min. Samples were acidified by adding phosphoric acid (final concentration ~2.5%). Binding buffer (100 mM TEAB in 90% methanol, 165 μL) was added to each tube, and the total contents were transferred to s-Trap columns. These tubes were spun at 4000 g for 1 min, and the flow-through was discarded. Trapped proteins were washed three times with wash buffer (100 mM TEAB in 90% methanol). Sequencing grade trypsin (Thermo Scientific) was added to the trap (1:20 trypsin:protein ratio) in 30 μL of 100 mM TEAB. The S-trap columns were incubated at 37 °C overnight, and the digested peptides were then eluted sequentially with 100 mM TEAB, 0.1% formic acid and 50% acetonitrile. Pooled eluates were dried in SpeedVac, and samples were reconstituted in 25 μL of 0.1% formic acid solution.

An externally calibrated Thermo Q Exactive Plus (high-resolution electrospray tandem mass spectrometer) was used in conjunction with a Dionex UltiMate3000 RSLCnano System. A 2 μL (1 μg equivalent) sample was aspirated into a 50 μL loop and loaded onto the trap column (Thermo μ-Precolumn 5 mm, with nanoViper tubing 30 μM i.d. × 10 cm). The flow rate was set to 300 nL/min for separation on the analytical column (Acclaim PepMap RSLC 75 μM × 15 cm nanoviper). Mobile phase A was composed of 99.9% H_2O (EMD Omni Solvent), and 0.1% formic acid and mobile phase B was composed of 0.1% formic acid in acetonitrile. A 120-min linear gradient from 3% to 45% B was performed. The LC eluent was directly nanosprayed into the mass spectrometer. During the chromatographic separation, the Q Exactive Plus was operated in a data-dependent mode and under direct control of the Thermo Excalibur 3.1.66 (Thermo Scientific). MS data were acquired using the following parameters: 15 data-dependent collisional-induced-dissociation (CID) MS/MS scans per full scan (400 to 1800 m/z) at 70,000 resolutions. MS2 was acquired at 17,500 resolutions. Ions with a single charge or charges of more than 7, as well as unassigned charges, were excluded. A 10 s dynamic exclusion window was used. All measurements were performed at room temperature.

Resultant Raw files were searched with Proteome Discoverer 3.0 using Sequest™ HT as the search engine using species-specific FASTA with 10 ppm error tolerance. Percolator was used as a peptide validator with 1% FDR (False Discovery Rate) as a cutoff.

Statistical analysis

Individual group effects were assessed using a Bayesian one-way ANOVA implemented via *stan_glm*. Unlike frequentist methods that rely on repeated-sampling assumptions and multiple-test corrections, Bayesian parameter estimation jointly samples the full posterior distribution of all model parameters. This approach provides a coherent probabilistic framework for inference without the need for post hoc adjustments. Hypothesis evaluation was based on the posterior probability mass within a specified parameter region, yielding a direct probability statement about the credibility of an effect[42,66–69].

All models were constructed using a fully hierarchical Bayesian approach with the *rstanarm* package (version 2.21.1) in R (version 4.0.3). The *rstanarm* package fits regression models in *stan*, using Hamiltonian Markov Chain Monte Carlo sampling to obtain credible estimates of model parameters. For both intercepts and predictors, we specified Student's *t*-distribution priors centered at zero with four degrees of freedom. The prior scale was set to 10 for intercepts and 2.5 for predictor variables. Each model was executed using four independent chains, with 500 warm-up iterations followed by 10,000 sampling iterations; every second sample was discarded (thinning). Details of the model evaluation and validation procedures are provided in our earlier publications[42,66–69]. In summary, all parameters had effective sample sizes greater than 2000, and convergence was verified by ensuring that the Gelman–Rubin shrinkage diagnostic was below 1.05 for all reported parameters. Visual inspection of trace plots confirmed good stationarity and mixing, and numerical checks supported successful convergence.

Credible intervals were summarized using the 95% highest posterior density interval (HDI), in which parameter values inside the interval are deemed more plausible given the data than those outside. Comparisons between groups were made by examining the overlap or lack thereof between posterior distributions of contrasts of interest, such as mean differences. When the HDI of the posterior difference distribution excluded zero, this was taken as evidence that the model-predicted means for the two conditions diverged, supporting the interpretation that the underlying parameters differed significantly (denoted by *).

Reporting summary

Further information on research design is available in the Nature Portfolio Reporting Summary linked to this article.

Data availability

All data supporting the findings of this study are available within the paper and its Supplementary Information. Data are available in Figshare with the identifier https://doi.org/10.6084/m9.figshare.

25690338, mass spectrometry proteomics data have been deposited to the ProteomeXchange Consortium via the PRIDE partner repository with the dataset identifier PXD070605, and the public repository https://github.com/housleylab/sangs_2025. Source data is available for Figs. 1–7 and Supplementary Figs. 1-3, 5, 9, 12, 15, 17, 19, 20-23 in the associated source data file. Source data are provided with this paper.

Code availability

All code are available in the public repository https://github.com/housleylab/sangs_2025.

References

1. Fire, A. et al. Potent and specific genetic interference by double-stranded RNA in *Caenorhabditis elegans*. *Nature* **391**, 806–811 (1998).
2. Hannon, G. J. RNA interference. *Nature* **418**, 244–251 (2002).
3. Tiemann, K. & Rossi, J. J. RNAi-based therapeutics–current status, challenges and prospects. *EMBO Mol. Med.* **1**, 142–151 (2009).
4. Warner, K. D., Hajdin, C. E. & Weeks, K. M. Principles for targeting RNA with drug-like small molecules. *Nat. Rev. Drug Discov.* **17**, 547–558 (2018).
5. Vargason, A. M., Anselmo, A. C. & Mitragotri, S. The evolution of commercial drug delivery technologies. *Nat. Biomed. Eng.* **5**, 951–967 (2021).
6. Setten, R. L., Rossi, J. J. & Han, S. -p The current state and future directions of RNAi-based therapeutics. *Nat. Rev. Drug Discov.* **18**, 421–446 (2019).
7. Hu, B. et al. Therapeutic siRNA: state of the art. *Signal Transduct. Target. Ther.* **5**, 101 (2020).
8. Urban-Klein, B., Werth, S., Abuharbeid, S., Czubayko, F. & Aigner, A. RNAi-mediated gene-targeting through systemic application of polyethylenimine (PEI)-complexed siRNA in vivo. *Gene Ther.* **12**, 461–466 (2005).
9. Wittrup, A. et al. Visualizing lipid-formulated siRNA release from endosomes and target gene knockdown. *Nat. Biotechnol.* **33**, 870–876 (2015).
10. Sahay, G. et al. Efficiency of siRNA delivery by lipid nanoparticles is limited by endocytic recycling. *Nat. Biotechnol.* **31**, 653–658 (2013).
11. Rietwyk, S. & Peer, D. Next-generation lipids in RNA interference therapeutics. *ACS Nano* **11**, 7572–7586 (2017).
12. Semple, S. C. et al. Rational design of cationic lipids for siRNA delivery. *Nat. Biotechnol.* **28**, 172–176 (2010).
13. Nguyen, L. N. et al. The mechanisms of nanoparticle delivery to solid tumours. *Nat. Rev. Bioeng.* **2**, 201–213 (2024).
14. Lokugamage, M. P. et al. Mild innate immune activation overrides efficient nanoparticle-mediated RNA delivery. *Adv. Mater.* **32**, 1904905 (2020).
15. Paunovska, K. et al. Analyzing 2000 in vivo drug delivery data points reveals that cholesterol structure impacts nanoparticle delivery. *ACS Nano* **12**, 8341–8349 (2018).
16. Paunovska, K., Loughrey, D. & Dahlman, J. E. Drug delivery systems for RNA therapeutics. *Nat. Rev. Genet.* **23**, 265–280 (2022).
17. Paunovska, K. et al. A direct comparison of in vitro and in vivo nucleic acid delivery mediated by hundreds of nanoparticles reveals a weak correlation. *Nano Lett.* **18**, 2148–2157 (2018).
18. Zuckerman, J. E. & Davis, M. E. Clinical experiences with systemically administered siRNA-based therapeutics in cancer. *Nat. Rev. Drug Discov.* **14**, 843–856 (2015).
19. Hattab, D., Gazzali, A. M. & Bakhtiar, A. Clinical advances of siRNA-based nanotherapeutics for cancer treatment. *Pharmaceutics* **13**, 1009 (2021).
20. Gustafson, H. H., Holt-Casper, D., Grainger, D. W. & Ghandehari, H. Nanoparticle uptake: the phagocyte problem. *Nano Today* **10**, 487–510 (2015).
21. Tai, W. Y. & Gao, X. H. Ribonucleoprotein: a biomimetic platform for targeted siRNA delivery. *Adv. Funct. Mater.* **29**, 1902221 (2019).
22. Tagalakis, A. D. et al. PEGylation improves the receptor-mediated transfection efficiency of peptide-targeted, self-assembling, anionic nanocomplexes. *J. Control. Release* **174**, 177–187 (2014).
23. Lv, H. T., Zhang, S. B., Wang, B., Cui, S. H. & Yan, J. Toxicity of cationic lipids and cationic polymers in gene delivery. *J. Control. Release* **114**, 100–109 (2006).
24. Kumar, R. et al. Efficient polymer-mediated delivery of gene-editing ribonucleoprotein payloads through combinatorial design, parallelized experimentation, and machine learning. *ACS Nano* **14**, 17626–17639 (2020).
25. Fang, Y. et al. Cleavable PEGylation: a strategy for overcoming the "PEG dilemma" in efficient. *Drug Deliv. Drug Deliv.* **24**, 22–32 (2017).
26. Miteva, M. et al. Tuning PEGylation of mixed micelles to overcome intracellular and systemic siRNA delivery barriers. *Biomaterials* **38**, 97–107 (2015).
27. Correa, S. et al. Tuning nanoparticle interactions with ovarian cancer through layer-by-layer modification of surface chemistry. *ACS Nano* **14**, 2224–2237 (2020).
28. Li, J. & Kataoka, K. Chemo-physical strategies to advance the in vivo functionality of targeted nanomedicine: the next generation. *J. Am. Chem. Soc.* **143**, 538–559 (2020).
29. Vaughan, H. J., Green, J. J. & Tzeng, S. Y. Cancer-targeting nanoparticles for combinatorial nucleic acid delivery. *Adv. Mater.* **32**, 1901081 (2020).
30. Blackburn, W. H., Dickerson, E. B., Smith, M. H., McDonald, J. F. & Lyon, L. A. Peptide-functionalized nanogels for targeted siRNA delivery. *Bioconjug. Chem.* **20**, 960–968 (2009).
31. Gan, D. & Lyon, L. A. Tunable swelling kinetics in core-shell hydrogel nanoparticles. *J. Am. Chem. Soc.* **123**, 7511–7517 (2001).
32. Jones, C. D. & Lyon, L. A. Synthesis and characterization of multi-responsive core– shell microgels. *Macromolecules* **33**, 8301–8306 (2000).
33. Satpathy, M., Mezencev, R., Wang, L. & McDonald, J. F. Targeted in vivo delivery of EGFR siRNA inhibits ovarian cancer growth and enhances drug sensitivity. *Sci. Rep.* **6**, 36518 (2016).
34. Liu, S.-L. et al. Visualizing the endocytic and exocytic processes of wheat germ agglutinin by quantum dot-based single-particle tracking. *Biomaterials* **32**, 7616–7624 (2011).
35. Raub, T. J., Koroly, M. J. & Roberts, R. M. Endocytosis of wheat germ agglutinin binding sites from the cell surface into a tubular endosomal network. *J. Cell. Physiol.* **143**, 1–12 (1990).
36. Chen, Y. et al. Targeting Xkr8 via nanoparticle-mediated in situ co-delivery of siRNA and chemotherapy drugs for cancer immunochemotherapy. *Nat. Nanotechnol.* **18**, 193–204 (2023).
37. Maeda, H. Toward a full understanding of the EPR effect in primary and metastatic tumors as well as issues related to its heterogeneity. *Adv. Drug Deliv. Rev.* **91**, 3–6 (2015).
38. Finn, J. D. et al. A single administration of CRISPR/Cas9 lipid nanoparticles achieves robust and persistent in vivo genome editing. *Cell Rep.* **22**, 2227–2235 (2018).
39. Benezra, M. et al. Multimodal silica nanoparticles are effective cancer-targeted probes in a model of human melanoma. *J. Clin. Invest.* **121**, 2768–2780 (2011).
40. Sheng, Q. & Liu, J. The therapeutic potential of targeting the EGFR family in epithelial ovarian cancer. *Br. J. Cancer* **104**, 1241–1245 (2011).
41. Teplinsky, E. & Muggia, F. EGFR and HER2: is there a role in ovarian cancer? *Translat. Cancer Res.* https://doi.org/10.3978/j.issn.2218-676X.2015.01.01 (2015).
42. Housley, S. N. et al. Cancer exacerbates chemotherapy-induced sensory neuropathy. Cancer Res. **80**, 2940–2955 (2020).
43. Ahuja, P., Sarkar, R., Vasos, P. R. & Bodenhausen, G. Diffusion coefficients of biomolecules using long-lived spin states. *J. Am. Chem. Soc.* **131**, 7498–7499 (2009).

44. Zheng, G. & Price, W. S. Simultaneous convection compensation and solvent suppression in biomolecular NMR diffusion experiments. *J. Biomol. NMR* **45**, 295–299 (2009).
45. Vallurupalli, P., Sekhar, A., Yuwen, T. R. & Kay, L. E. Probing conformational dynamics in biomolecules via chemical exchange saturation transfer: a primer. *J. Biomol. NMR* **67**, 243–271 (2017).
46. Hincapie, R. et al. Multivalent targeting of the asialoglycoprotein receptor by virus-like particles. *Small* **19**, 2304263 (2023).
47. Rosenblum, D., Joshi, N., Tao, W., Karp, J. M. & Peer, D. Progress and challenges towards targeted delivery of cancer therapeutics. *Nat. Commun.* **9**, 1410 (2018).
48. Kingston, B. R. et al. Specific endothelial cells govern nanoparticle entry into solid tumors. *ACS Nano* **15**, 14080–14094 (2021).
49. Sindhwani, S. et al. The entry of nanoparticles into solid tumours. *Nat. Mater.* **19**, 566–575 (2020).
50. Boehnke, N. et al. Massively parallel pooled screening reveals genomic determinants of nanoparticle delivery. *Science* **377**, eabm5551 (2022).
51. Chen, Q. R. et al. Meta-analysis of nanoparticle distribution in tumors and major organs in tumor-bearing mice. *ACS Nano* **17**, 19810–19831 (2023).
52. Watanabe, S. et al. In vivo rendezvous of small nucleic acid drugs with charge-matched block catiomers to target cancers. *Nat. Commun.* **10**, 1894 (2019).
53. Dreher, M. R. et al. Tumor vascular permeability, accumulation, and penetration of macromolecular drug carriers. *J. Nat. Cancer Inst.* **98**, 335–344 (2006).
54. Less, J. R., Posner, M. C., Skalak, T. C., Wolmark, N. & Jain, R. K. Geometric resistance and microvascular network architecture of human colorectal carcinoma. *Microcirculation* **4**, 25–33 (1997).
55. Sevick, E. M. & Jain, R. K. Geometric resistance to blood flow in solid tumors perfused ex vivo: effects of tumor size and perfusion pressure. *Cancer Res* **49**, 3506–3512 (1989).
56. Chauhan, V. P., Stylianopoulos, T., Boucher, Y. & Jain, R. K. Delivery of molecular and nanoscale medicine to tumors: transport barriers and strategies. *Annu. Rev. Chem. Biomol. Eng.* **2**, 281–298 (2011).
57. Fukumura, D. & Jain, R. K. Tumor microenvironment abnormalities: causes, consequences, and strategies to normalize. *J. Cell. Biochem.* **101**, 937–949 (2007).
58. Bresette, C. A. et al. Novel tubing connectors reduce ECMO circuit thrombosis. *Int. J. Artif. Organs* **47**, 347–355 (2024).
59. Ruoslahti, E., Bhatia, S. N. & Sailor, M. J. Targeting of drugs and nanoparticles to tumors. *J. Cell Biol.* **188**, 759–768 (2010).
60. Poon, W., Kingston, B. R., Ouyang, B., Ngo, W. & Chan, W. C. W. A framework for designing delivery systems. *Nat. Nanotechnol.* **15**, 819–829 (2020).
61. Subhan, M. A., Yalamarty, S. S. K., Filipczak, N., Parveen, F. & Torchilin, V. P. Recent advances in tumor targeting via EPR effect for cancer treatment. *J. Pers. Med.* **11**, 571 (2021).
62. Koshrovski-Michael, S. et al. Two-in-one nanoparticle platform induces a strong therapeutic effect of targeted therapies in P-selectin-expressing cancers. *Sci. Adv.* **10**, eadr4762 (2024).
63. Costes, S. V. et al. Automatic and quantitative measurement of protein-protein colocalization in live cells. *Biophys. J.* **86**, 3993–4003 (2004).
64. Das, S. et al. Stabilization of near-infrared fluorescent proteins by packaging in virus-like particles. *Biomacromolecules* **21**, 2432–2439 (2020).
65. Pustulka, S. M., Ling, K., Pish, S. L. & Champion, J. A. Protein nanoparticle charge and hydrophobicity govern protein corona and macrophage uptake. *ACS Appl. Mater. Interfaces* **12**, 48284–48295 (2020).
66. Horstman, G. M., Housley, S. N. & Cope, T. C. Dysregulation of mechanosensory circuits coordinating the actions of antagonist motor pools following peripheral nerve injury and muscle reinnervation. Exp. Neurol. **318**, 124–134 (2019).
67. Housley, S. N., Nardelli, P., Powers, R. K., Rich, M. M. & Cope, T. C. Chronic defects in intraspinal mechanisms of spike encoding by spinal motoneurons following chemotherapy. Exp. Neurol. **331**, 113354 (2020).
68. Housley, S. N., Nardelli, P., Rotterman, T. M. & Cope, T. C. Neural circuit mechanisms of sensorimotor disability in cancer treatment. Proc. Natl. Acad. Sci. USA **118**, e2100428118 (2021).
69. Rotterman, T. M. et al. Axon initial segment geometry in relation to motoneuron excitability. *PloS one* **16**, e0259918 (2021).

Acknowledgments

This work was supported by the McCallum Early Career Award (S.N.H.), grants from the Northside Hospital Foundation, Inc. (S.N.H.), Ovarian Cancer Institute (S.N.H.), Georgia Research Alliance (S.N.H. and J.F.M.), the Deborah Nash Endowment, NSF Award 2338466 (V.J. and I.A.P.) and National Cancer Institute R01CA221363 (S.N.H.). We acknowledge the animal support staff at the two institutions: Georgia Institute of Technology Physiological Research Laboratory (PRL) and Global Center for Medical Innovation T3 Labs. We thank the pathology core facilities at the Yerkes National Primate Research Center for histology and tissue preparation work. We acknowledge the Systems Mass Spectrometry Core at the Institute of Bioengineering and Bioscience, Georgia Institute of Technology, with special thanks to Ludyanna Lebon and Dr. Rakesh Singh for their expertise and support. We thank the Nanotechnology Characterization Laboratory (NCL) for performing independent nanoparticle analyses.

Author contributions

S.N.H. conceived and supervised this project. S.N.H. conceived the SANG mechanism. S.N.H., M.G.F., J.E.D., and V.J. conceptualized experiments. S.N.H., A.R.B. synthesized SANGs. S.N.H., A.R.B., and L.V.M. performed in vitro studies. S.N.H., A.R.B., and E.S.E. performed in vivo studies. I.A.P. performed LP-TEM studies. J.C.A. performed EM studies. M.I. performed protein corona incubations. J.F.M. lab synthesized early nanoparticles for NCL. S.N.H., E.S.E., and I.A.P. curated data. S.N.H., E.S.E., S.L., and O.A.H., performed analyses. S.N.H., M.G.F., E.S.E., and I.A.P. generated visualizations. S.N.H. wrote the original manuscript. S.N.H., M.G.F., and A.R.B. reviewed and edited the manuscript before submission.

Competing interests

S.N.H., J.F.M., and M.G.F. have a provisional patent filing (Application No. 63/517,215) related to this work. This study could affect their personal financial statuses. The terms of these arrangements have been reviewed and approved by The Georgia Institute of Technology in accordance with its conflict-of-interest policies. All other authors declare no competing interests.

Additional information

Supplementary information The online version contains supplementary material available at https://doi.org/10.1038/s41467-025-66788-4.

Correspondence and requests for materials should be addressed to Stephen N. Housley.

Peer review information *Nature Communications* thanks Heemin Kang and the other anonymous reviewer(s) for their contribution to the peer review of this work. [A peer review file is available].